NLOS-Aided Joint OTA Synchronization and Off-Grid Imaging for Distributed MIMO Systems

Citation for the original published paper (version of record):
Tong, X., Zhang, L., Ge, Y. et al (2026). NLOS-Aided Joint OTA Synchronization and Off-Grid Imaging for Distributed MIMO Systems. IEEE Transactions on Wireless Communications, In Press.
http://dx.doi.org/10.1109/TWC.2026.3732875

NLOS-Aided Joint OTA Synchronization and Off-Grid Imaging for Distributed MIMO Systems

Xin Tong, *Member, IEEE*, Lechen Zhang, *Graduate Student Member, IEEE*, Yu Ge, *Member, IEEE*, Dario Tagliaferri, *Member, IEEE*, and Henk Wymeersch, *Fellow, IEEE*

***Abstract*—Distributed multiple-input multiple-output (MIMO) architectures enable large-scale integrated sensing and communication (ISAC) by providing high spatial resolution and robustness through spatial diversity. However, practical phase-coherent sensing is challenged by phase synchronization errors and modeling mismatch caused by grid discretization. Existing over-the-air (OTA) synchronization methods typically treat synchronization and sensing tasks separately, which may lead to inaccurate phase alignment when multipath components are used for imaging. In this paper, we propose a non-line-of-sight (NLOS)-aided joint OTA synchronization and off-grid imaging framework for distributed MIMO ISAC systems. First, a line-of-sight (LOS)-assisted coarse synchronization is performed to establish initial phase coherence across distributed links. Subsequently, an iterative refinement stage exploits reconstructed NLOS components obtained from imaging results. By modeling off-grid effects via a first-order Taylor expansion, we transform measurements with nonlinear off-grid offset into an augmented linear model with jointly sparse reflectivity and off-set variables. The imaging problem is reformulated as a structured sparse recovery task and solved using a tailored off-grid approximate message passing (OG-AMP) algorithm. The imaging and synchronization modules are coupled within a closed-loop alternative optimization framework, where improved imaging enables more accurate phase refinement, and vice versa. Numerical results show that the proposed framework achieves accurate synchronization and imaging under phase errors. Compared with conventional approaches, it shows superior robustness and accuracy.**

***Index Terms*—Distributed multiple-input multiple-output (MIMO), integrated sensing and communication (ISAC), over-the-air (OTA) synchronization, off-grid imaging.**

I. Introduction

In FUTURE integrated sensing and communication (ISAC) systems, the distributed multiple-input multiple-output (MIMO) architecture is considered as a key factor in achieving large-scale environment sensing, supporting applications such as intelligent transportation, extended reality, and ubiquitous environmental monitoring [1], [2]. In such systems, large-scale deployment of spatially separated transmitters (Txs) and receivers (Rxs) enables unprecedented sensing resolution and communication reliability. In practice, such systems operate in complex propagation environments where line-of-sight (LOS) and abundant non-line-of-sight (NLOS) multipath components coexist. While this poses challenges for over-the-air (OTA) synchronization and phase-coherent sensing, the joint presence of LOS and NLOS paths also provides new opportunities to exploit multipath diversity for synchronization and sensing within a unified OTA framework [3], [4].

The first challenge arises from the tight synchronization requirement in distributed MIMO systems [5]. Each transceiver has its own clock and oscillator, leading to time offsets (TOs) and phase offsets (POs), which can have an impact on multiple links. These residual offsets distort phase-sensitive measurements and severely degrade coherent processing such as beam-focusing or multi-static imaging [6]. Although wired synchronization via fiber-optic links is technically feasible for small-scale arrays, the hardware cost becomes prohibitively expensive when scaled over a large number of sensors, limiting flexible node deployment [7]. Moreover, while wired links effectively facilitate data sharing and coordination, the level of synchronization needed for standard communication is much more relaxed than the sub-wavelength phase alignment required for multi-static coherent imaging. Therefore, wireless OTA synchronization remains an indispensable alternative to eliminate residual POs in scalable distributed MIMO ISAC architectures. In practice, LOS paths are commonly exploited to provide a coarse synchronization reference. However, LOS-based synchronization alone is often unreliable in realistic distributed MIMO scenarios due to occlusions, intermittent visibility, and limited geometric diversity [8], [9], [10]. Thus, there is a strong need for robust synchronization that can operate with abundant NLOS links.

Another challenge arises from POs introduced by the mismatch between grid-based imaging models and the continuous physical environment. In large-scale sensing, the region of interest is commonly discretized into coarse grid of pixels to control computational complexity [11]. As a result, the main scattering centers rarely coincide with grid center points, leading to off-grid modeling errors. For imaging, such off-grid offsets partly manifest as phase variations in the scattering coefficients and also affect the accuracy of coherent processing. Moreover, when the reconstructed data is further used for refined synchronization, these off-grid-induced POs are

Received 5 March 2026; revised 7 July 2026; accepted 6 September 2026. Date of publication 11 September 2026; date of current version 22 September 2026. This work was supported in part by the Smart Networks and Services Joint Undertaking (SNS JU) Project 6G for Distributed Intelligent Sensing and Communication (6G-DISAC) through the European Union (EU) Horizon Europe Research and Innovation Program under Grant 101139130, in part by Swedish Research Council under Grant 2022-03007, and in part by the Horizon Europe Marie Skłodowska-Curie Actions (HORIZON-MSCA) Multi-View Intelligent Collaborative Communication and Sensing for 6G Networks (MICCAS-6G) Project under Grant 101275066. The associate editor coordinating the review of this article and approving it for publication was G. Zhu. *(Corresponding author: Yu Ge.)*

Xin Tong, Yu Ge, and Henk Wymeersch are with the Department of Electrical Engineering, Chalmers University of Technology, 41296 Gothenburg, Sweden (e-mail: xinto@chalmers.se; yuge@chalmers.se; henkw@chalmers.se).

Lechen Zhang is with the National Key Laboratory of Wireless Communications, University of Electronic Science and Technology of China, Chengdu 611731, China (e-mail: zhanglechen@std.uestc.edu.cn).

Dario Tagliaferri is with the Department of Electronics, Information and Bioengineering, Politecnico di Milano, 20133 Milan, Italy (e-mail: dario.tagliaferri@polimi.it).

Digital Object Identifier 10.1109/TWC.2026.3732875

fundamentally indistinguishable from those caused by imperfect synchronization, making coherent processing particularly challenging [12]. While using extremely fine grids could reduce such phase errors, the resulting memory and computational overhead makes this method impractical. Importantly, in NLOS-rich environments, multipath propagation will provide more geometrically diverse measurements that can be used for joint synchronization and imaging.

Motivated by these challenges, this paper proposes a NLOS-aided ISAC framework that integrates LOS-based coarse synchronization with NLOS-assisted joint refinement and off-grid imaging in distributed MIMO systems. In the joint framework, synchronization and imaging are are equally important inherently interdependent. Accurate phase-coherent imaging requires phase-level alignment, while reliable imaging results offer environmental features to refine synchronization. Furthermore, such high-precision synchronization is essential to support other critical applications in distributed MIMO systems.

A. Related Works

From the perspective of sensing methods in ISAC systems, conventional imaging techniques have been widely studied, such as radar-based imaging [13], [14], phased-array beamspace imaging [15], and multistatic coherent imaging [16], [17]. Compared with pure localization or parameter estimation, imaging-based sensing provides a richer and more interpretable representation of the environment, enabling the extraction of spatial structures, target shapes and sizes, and scattering distributions that are highly beneficial for ISAC. However, these model-driven linear imaging methods are limited by the sidelobe structure of the resulting point spread function, while computational imaging methods can improve performance by leveraging sparsity priors [18]. Although distributed ISAC architectures provide increased spatial degrees of freedom through geographically separated nodes, classical linear imaging methods do not fully exploit this advantage. In dense NLOS environments commonly encountered in ISAC systems, classical imaging models either become inaccurate or require increasingly complex propagation modeling, and the resulting images often lack fine spatial resolution.

To overcome these limitations, computational imaging has recently emerged as a powerful alternative for wireless environment sensing [19]. By dividing the scenario into discrete pixels and recovering their scattering coefficients, computational imaging transforms the sensing task into a sparse reconstruction problem that can achieve high-resolution imaging even with limited physical resources. In addition, compared to classical linear imaging methods, computational imaging provides a more flexible framework and accurate results for ISAC. By passively reusing communication signals, it avoids interference with the communication process. Based on compressed sensing theory [20], various sparse reconstruction algorithms, such as the orthogonal matching pursuit (OMP) algorithm [21] and the generalized approximate message passing (GAMP) algorithm [22], have been applied to MIMO orthogonal frequency division multiplexing (OFDM) sensing [23] and millimeter-wave communication environment reconstruction [24], [25]. These methods demonstrate the great potential of computational imaging as a fundamental feature of future ISAC systems.

Despite these advantages, existing computational imaging methods are typically developed under the assumption of ideal synchronization. In practical distributed ISAC systems, TOs and POs can severely degrade imaging performance. To address this issue, map-assisted or multipath-assisted synchronization techniques have been proposed to improve coherence among distributed transceivers. For instance, [3] shows that environmental information can effectively reduce time and phase misalignment in distributed MIMO systems, with related ideas applied to cell-free massive MIMO [5], multistatic radar [26], and cooperative localization [27]. However, existing synchronization approaches are generally developed independently of imaging and often rely on either strong LOS components or accurate prior map information. The lack of a unified framework that jointly integrates imaging and synchronization limits their applicability in practical large-scale ISAC systems.

B. Contributions

In this paper, we propose joint OTA synchronization and environment imaging in distributed MIMO ISAC systems operating in NLOS-rich scenarios. Different from conventional approaches that address synchronization and sensing separately, we aim to exploit abundant NLOS multipath components as a shared resource for both synchronization and imaging. Specifically, we first formulate a unified OFDM signal model that captures both synchronization POs and off-grid scattering effects within a common computational imaging framework. We exploit available LOS components to obtain a coarse estimation of POs across distributed transceivers. Building upon this initial synchronization, we perform sparse environment imaging using NLOS multipath components. Based on message passing theory, off-grid approximate message passing (OG-AMP) algorithm is proposed to reconstruct sparse NLOS scattering structures. Unlike existing approximate message passing (AMP) algorithms primarily designed for standard sparse estimation tasks such as channel estimation [28] and symbol detection [29], the proposed OG-AMP method introduces a unique structural prior tailored for high-resolution computational imaging. Specifically, it enforces a grid-level coupling constraint, ensuring that the target's scattering coefficient and its corresponding off-grid offset share the exact same spatial grid index. This structure effectively exploits the physics of grid-based imaging, preventing the estimated parameters from diverging. This imaging result enables the estimation and refinement of OTA synchronization parameters. The updated synchronization parameters in turn improves phase coherence across links, leading to progressively more accurate imaging results. In summary, the complete procedure of the proposed framework operates in a closed-loop manner: first, a robust LOS-assisted coarse synchronization provides the initial phase alignment; second, based on this initialization, the OG-AMP module reconstructs the environmental scatterers while correcting grid mismatches; third, the imaging results are fed back as virtual anchors to perform NLOS-aided synchronization refinement, which in turn improves the next round of imaging. Through this alternative optimization (AO) between imaging and synchronization, the proposed method enables reliable joint sensing and synchronization in ISAC systems. The main contributions of this work are summarized as follows:

- We propose a unified OFDM-based ISAC framework that jointly performs OTA phase synchronization and environment imaging by passively exploiting channel state information (CSI) obtained from the standard communication process. Instead of treating NLOS multipath as interference, the proposed method leverages those paths as virtual anchors to support both synchronization and sensing in distributed MIMO systems.
- An OG-AMP imaging algorithm is proposed to explicitly account for model mismatch caused by coarse grids and residual synchronization errors. The proposed method is able to reliably recover sparse scattering structures even when phase-level errors are present, which is particularly important in large-scale NLOS scenarios.
- We further propose an OTA synchronization strategy that constructs an ideal reference channel from the reconstructed NLOS imaging results. By comparing the received signals with this reference, residual POs can be iteratively refined, forming an AO between imaging and synchronization.
- Simulation results demonstrate that, in scenarios where conventional processing methods fail or provide unreliable estimates, the proposed approach achieves effective performance gains for both synchronization and imaging, highlighting its practical value for ISAC deployments.

The rest of this paper is organized as follows. Section II presents the environment setting and system model. Section III details the OTA synchronization method. Section IV develops the tailored OG-AMP imaging algorithm. Section V provides the theoretical analysis. Finally, Section VI presents the numerical results, and Section VII concludes the paper.

Notation: Fonts a, $\boldsymbol{a}$, and $\mathbf{A}$ represent scalars, vectors, and matrices, respectively. $\mathbf{A}^{\mathsf{T}}$ and $\|\mathbf{A}\|_{\mathrm{F}}$ denote transpose and Frobenius norm of $\mathbf{A}$, respectively. $|\cdot|$ and $[\cdot]$ denote the modulus and the catenation of the matrix, respectively. $\circ$ and $\otimes$ represents the Hadamard product and the Kronecker product between two matrices, respectively. Finally, notation $\mathrm{diag}(\boldsymbol{a})$ represents a diagonal matrix with the entries of $\boldsymbol{a}$ on its main diagonal, and $\delta(\cdot)$ is the Dirac delta function.

II. System Model

A. Environment Setting

We consider the distributed MIMO ISAC system in Fig. 1, including multiple spatially distributed Tx and Rx nodes, each with a single, isotropic antenna. All antennas are connected to a central processing unit (CPU). All Tx and Rx nodes are connected through the available links and the CPU acts as a fusion center, aggregating the CSI from all distributed links to perform joint high-resolution imaging. The imaging results were then used to improve OTA synchronization, and

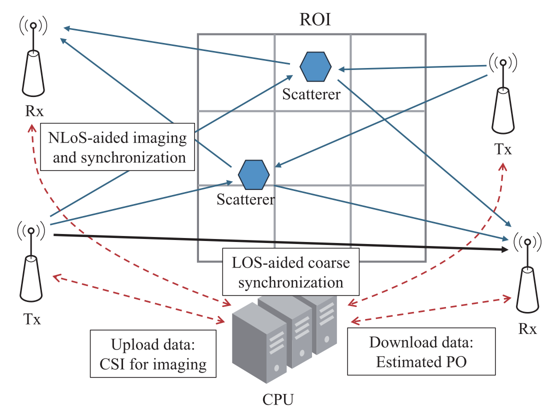

Fig. 1. A joint OTA synchronization and imaging scenario in disributed MIMO systems.

each distributed Tx-Rx link was calibrated on the CPU to compensate for the estimated synchronization error.[1]

In the distributed architecture, each ISAC node operates with an independent local oscillator (LO). The independent LOs in distributed nodes introduce relative clock offsets due to hardware imperfections. As a result, each Tx-Rx link presents an unknown TO, which further induces a random uniformly-distributed carrier PO after downconversion. These POs are absorbed into the effective response and severely degrade the phase coherence required for high-resolution imaging.

In conventional OFDM communication systems, synchronization is typically performed on each Tx-Rx link basis. Coarse timing estimation is achieved using cyclic prefixes (CPs) or predefined preambles, followed by frequency-domain channel estimation and data demodulation, which absorbs both LOS and NLOS multipath components into composite subcarrier coefficients [30]. This level of synchronization is generally sufficient for communication systems, where knowledge of absolute delays and phases is not required, as long as these impairments remain quasi-static and channel reciprocity holds. In contrast, distributed MIMO sensing requires synchronization across multiple Txs and Rxs. Coherent imaging critically relies on consistent phase information across links and subcarriers.

B. Grid-Based Signal Model

Each Tx employs a standard OFDM signaling scheme, and transmits data symbols together with predefined pilot symbols over K orthogonal subcarriers with subcarrier spacing Δf and a CP. Different Txs are multiplexed using orthogonal communication resources so that their individual CSI can be reliably estimated at the Rxs following conventional OFDM-based channel estimation procedures. No sensing-oriented waveform or dedicated probing signal is designed in this work, focusing on a complete reuse of OFDM signals. The proposed framework passively exploits the CSI obtained from the standard communication process.

[1]Note that we assume the CPU aggregates the CSI from all nodes for joint processing but does not distribute a shared phase-coherent clock reference due to hardware and cost constraints, thereby requiring an effective OTA synchronization mechanism.

As shown in Fig. 1, we discretize the 2-dimensional (2D) region of interest (ROI) into pixels, where each pixel represents the mean centroid of scatterers and an average scattering coefficient within that pixel.[2] We use the scattering coefficient x_n to represent the environmental information in the n-th pixel. If no target object in n-th pixel, $x_n = 0$. Otherwise, we have $x_n \in (0, 1]$, which is normalized according to a maximum value of expected environment reflectivity and the total number of pixels is denoted as N. Therefore, the environmental information of the ROI can be characterized by the scattering coefficient vector $\boldsymbol{x} = [x_1, x_2, \ldots, x_N]^\mathsf{T}$. It is worth noting that $\boldsymbol{x}$ is a property of the environment itself, not related to the propagation path.

Existing environment-aided synchronization methods typically assume simplified point targets and full LOS visibility [3], [4]. Note that our framework does not strictly require all LOS paths to be visible, but rather a minimum of one direct LOS link per node to maintain network connectivity, meaning the method remains functional even when many links are blocked. Although practical deployments involve complex occlusions [25] and extended targets, this paper focuses on point scatterers to establish a baseline joint framework. Our goal is not to replace mainstream LOS-based coarse initialization, but to show how abundant NLOS paths can further improve phase estimates to meet the strict coherence needs of high-resolution imaging. Future work will extend this baseline framework to handle continuous geometric shapes and partial LOS blockages.

Let the center of the n-th pixel be $\boldsymbol{p}_n = [x_n, y_n]^\mathsf{T}$, Tx position $\boldsymbol{p}_{\mathrm{Tx},m} = [x_{\mathrm{Tx},m}, y_{\mathrm{Tx},m}]^\mathsf{T}$ and Rx position $\boldsymbol{p}_{\mathrm{Rx},m} = [x_{\mathrm{Rx},m}, y_{\mathrm{Rx}.m}]^\mathsf{T}$. The free-space propagation channel gain $a_{m,k}(\boldsymbol{p}_n)$ passing through the n-th pixel of the m-th Tx-Rx link is calculated as [31]

$$a_{m,k}(\boldsymbol{p}_n) = \frac{1}{L_m(\boldsymbol{p}_n)} \exp(-j2\pi f_k \tau_m(\boldsymbol{p}_n)), \tag{1}$$

where $f_k = f_c + k\Delta f$ is the frequency of the k-th subcarrier with f_c denotes carrier frequency. The propagation delay $\tau_m(\boldsymbol{p}_n)$ and the amplitude attenuation $L_m(\boldsymbol{p}_n)$ are

$$\tau_m(\boldsymbol{p}_n) = (\|\boldsymbol{p}_n - \boldsymbol{p}_{\mathrm{Tx},m}\|_2 + \|\boldsymbol{p}_n - \boldsymbol{p}_{\mathrm{Rx},m}\|_2)/c, \tag{2}$$
$$L_m(\boldsymbol{p}_n) = 4\pi\alpha(\|\boldsymbol{p}_n - \boldsymbol{p}_{\mathrm{Tx},m}\|_2 \cdot \|\boldsymbol{p}_n - \boldsymbol{p}_{\mathrm{Rx},m}\|_2)/\lambda_k, \tag{3}$$

which is assumed to be constant within the bandwidth, λ_k is the wavelength and α is the normalization constant that implicitly apply to $\boldsymbol{x}$.

Synchronization offsets originate at the node level rather than at the individual Tx-Rx link level. Specifically, we define the node-level baseband POs on the k-th subcarrier as [4]

$$\phi_{\mathrm{Tx},i,k} = 2\pi f_k\, \delta t_{\mathrm{Tx},i} + \phi_{\mathrm{LO,Tx},i}, \tag{4}$$
$$\phi_{\mathrm{Rx},j,k} = 2\pi f_k\, \delta t_{\mathrm{Rx},j} + \phi_{\mathrm{LO,Rx},j}, \tag{5}$$

where $\delta t_{\mathrm{Tx},i} \sim \mathrm{U}(0, 1/\Delta f)$ and $\delta t_{\mathrm{Rx},j} \sim \mathrm{U}(0, 1/\Delta f)$ denote the TOs of the i-th Tx and j-th Rx nodes, respectively, and $\phi_{\mathrm{LO,Tx},i} \sim \mathrm{U}(0, 2\pi)$ and $\phi_{\mathrm{LO,Rx},j} \sim \mathrm{U}(0, 2\pi)$ represent their LO-induced POs.

In this paper, we will estimate the global PO at the node level to achieve synchronization. The Tx PO enters the baseband signal through upconversion, while the Rx PO appears with an opposite sign due to downconversion using the conjugate local oscillator. The composite PO associated with the (i, j)-th Tx-Rx link can then be expressed as [7]

$$\Phi_{m,k} = \phi_{\mathrm{Tx},i,k} - \phi_{\mathrm{Rx},j,k}, \tag{6}$$

where m indexes the corresponding Tx-Rx link. It should be noted that minor errors in node positioning can be incorporated into the total PO item without loss of generality. Considering that the proposed method is a single-snapshot imaging method, residual carrier frequency offset (CFO) is incorporated into the constant PO. By stacking the node-level phase terms into a vector $\boldsymbol{\phi}_k = [\phi_{\mathrm{Tx},1,k}, \ldots, \phi_{\mathrm{Tx},N_{\mathrm{Tx}},k}, \phi_{\mathrm{Rx},2,k}, \ldots, \phi_{\mathrm{Rx},N_{\mathrm{Rx}},k}]^\mathsf{T} \in \mathbb{C}^{N_{\mathrm{Tx}}+N_{\mathrm{Rx}}-1}$, the link-level phase vector $\boldsymbol{\varphi}_k = [\Phi_{1,k}, \ldots, \Phi_{M,k}] \in \mathbb{C}^M$ is written as

$$\boldsymbol{\varphi}_k = \mathbf{G}\boldsymbol{\phi}_k \tag{7}$$

where $\mathbf{G} \in \{0, \pm 1\}^{M \times (N_{\mathrm{Tx}}+N_{\mathrm{Rx}}-1)}$ is the network incidence matrix, indicating that there are links (LOS or NLOS) between the corresponding Tx and Rx nodes, $M = N_{\mathrm{Tx}} \times N_{\mathrm{Rx}}$ is the number of links. For m-th link connecting Tx i and Rx j, the element corresponding to Tx node i is $+\,1$ and the element corresponding to Rx node j is -1. All other elements in m-th row are 0. It is worth noting that the absolute phase reference is unobservable, and therefore the phase of the node with the most links can be fixed as a reference phase. Note that If multiple nodes share the same maximum number of links, the node with the smallest index is chosen by default. In dynamic topologies, the system continuously updates the network connection matrix. Consequently, the total number of independent phase parameters is reduced from the number of nodes to $N_{\mathrm{Tx}} + N_{\mathrm{Rx}} - 1$. The CSI $y_{m,k}$ of the m-th Tx-Rx can be modeled as[3]

$$y_{m,k} = \left(h_{m,k}^{\mathrm{LOS}} u_m + \sum_{n=1}^{N} a_{m,k}(\boldsymbol{p}_n) x_n \right) \cdot e^{-j\Phi_{m,k}} + n_{m,k}, \tag{8}$$

where u_m is a known boolean visibility factor indicating whether the m-th link has a LOS path, $n_{m,k}$ represents the Gaussian noise. The LOS channel $h_{m,k}^{\mathrm{LOS}}$ is under free-space propagation assumption, as

$$h_{m,k}^{\mathrm{LOS}} = \frac{1}{L_m^{\mathrm{LOS}}} \exp(-j2\pi f_k \tau_m^{\mathrm{LOS}}), \tag{9}$$

where $\tau_m^{\mathrm{LOS}} = \|\boldsymbol{p}_{\mathrm{Tx},m} - \boldsymbol{p}_{\mathrm{Rx},m}\|_2/c$ is the LOS propagation delay. The LOS amplitude attenuation is calculated as $L_m^{\mathrm{LOS}} = 4\pi\|\boldsymbol{p}_{\mathrm{Tx},m} - \boldsymbol{p}_{\mathrm{Rx},m}\|_2/\lambda_k$, as for free-space propagation. The LOS path is not affected by scatterers and is therefore independent of the pixel grid.

In this paper, conventional channel estimation and equalization are performed to reliably recover the communication data [30]. The estimated CSI on all subcarriers is then passively reused for imaging, enabling ISAC without introducing

[2] The analysis method for 3-dimensional (3D) scenarios can be derived using a similar approach.

[3] Higher-order scattering effects are ignored and treated as noise due to their larger attenuation.

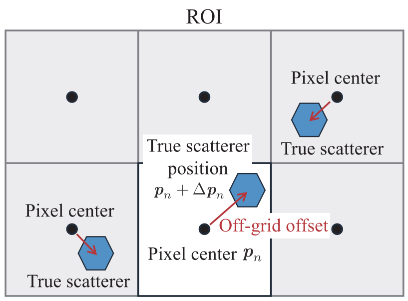

Fig. 2. A 2D pixel grid, with targets randomly distributed on the grid, exhibits the off-grid effect shown by the red arrow.

additional signaling overhead. We jointly process channel estimation results of M Tx-Rx links and K subcarriers, so (8) can be written in matrix form as

$$\boldsymbol{y} = \boldsymbol{\Phi}(\boldsymbol{h}^{\mathrm{LOS}} \circ \tilde{\boldsymbol{u}} + \mathbf{A}\boldsymbol{x}) + \boldsymbol{n}, \tag{10}$$

where $\boldsymbol{y} \in \mathbb{C}^{MK}$ is a stacked vector of all estimated channel propagation gains, $\boldsymbol{h}^{\mathrm{LOS}} \in \mathbb{C}^{MK}$ is the stacked vector of $h^{\mathrm{LOS}}_{m,k}$. Vector $\tilde{\boldsymbol{u}} = \boldsymbol{u} \otimes \mathbf{1}_K \in \mathbb{B}^{MK}$ and $\boldsymbol{u} \in \mathbb{B}^{M}$ is the stacked vector of u_m. Matrix $\boldsymbol{\Phi} = \mathrm{diag}([e^{-j\varphi_1}, \ldots, e^{-j\varphi_K}]) \in \mathbb{C}^{MK \times MK}$ is a diagonal matrix containing the POs on all Tx-Rx links and subcarriers. The free-space propagation gain matrix for all links and subcarriers is denoted as $\mathbf{A} \in \mathbb{C}^{MK \times N}$, used as the reference channel dictionary for imaging.

In this paper, we focus on the joint performance of OTA synchronization and imaging. As shown in (10), we consider the POs $\boldsymbol{\Phi}$ and environment information $\boldsymbol{x}$ as unknown variables to be solved, and the other reference propagation gains are known values. In addition, some novel propagation models have been proposed to more accurately describe wireless signal propagation in pixelated environments [11], [24], [25], [32]. These models can be used to replace the $\mathbf{A}$ model in (1) and extended to an off-grid model. For the propagation model, we focus on isotropic targets and we can apply other accurate models and consider other physical properties of pixels (e.g., shape of target, frequency dependence) in the future.

C. Off-Grid Approximation Model

In this section, we take a point scatterer as an example to illustrate the off-grid problem in imaging and propose an off-grid channel model as an extension of the grid-based channel model in Section II-B. Note that a pixel is the smallest unit of imaging. When there are multiple scatterers in a pixel, these sub-scatterers can be modeled as a single equivalent point scatterer with average intensity and average off-grid offset through coherent superposition of signals [33]. As shown in Fig. 2, the true scatterer is not exactly at the pixel center, which causes the different PO of each link. Consider a true scatterer located at $\boldsymbol{p}_n + \Delta\boldsymbol{p}_n$ instead of placed in the pixel center $\boldsymbol{p}_n$, where $\Delta\boldsymbol{p}_n$ is the off-grid offset. The reference propagation gain in (1) is approximated by first-order Taylor expansion

$$a_{m,k}(\boldsymbol{p}_n + \Delta\boldsymbol{p}_n) \approx a_{m,k}(\boldsymbol{p}_n) + (\nabla_{\boldsymbol{p}} a_{m,k}(\boldsymbol{p}_n))^{\mathsf{T}} \Delta\boldsymbol{p}_n. \tag{11}$$

Since the amplitude change is not significant under relatively small off-grid offsets $\Delta\boldsymbol{p}_n$, we consider only variation of the phase information [31]. Inspired by diffraction theory that the spatial gradient is determined by the transmit and receive wavevectors [16], the gradient of the position $\boldsymbol{p}_n$ is approximated as

$$\begin{aligned}&\nabla_{\boldsymbol{p}} a_{m,k}(\boldsymbol{p}_n)\\ &\approx \frac{\partial a_{m,k}}{\partial \tau_m} \nabla_{\boldsymbol{p}} \tau_m\\ &= -j\frac{2\pi}{\lambda_k} a_{m,k}(\boldsymbol{p}_n)\left(\frac{\boldsymbol{p}_n - \boldsymbol{p}_{\mathrm{Tx},m}}{\|\boldsymbol{p}_n - \boldsymbol{p}_{\mathrm{Tx},m}\|_2} + \frac{\boldsymbol{p}_n - \boldsymbol{p}_{\mathrm{Rx},m}}{\|\boldsymbol{p}_n - \boldsymbol{p}_{\mathrm{Rx},m}\|_2}\right).\end{aligned} \tag{12}$$

In 2D scenario, define the gradient reference channel gain matrices $\mathbf{A}_x = \partial\mathbf{A}/\partial x \in \mathbb{C}^{MK \times N}$ and $\mathbf{A}_y = \partial\mathbf{A}/\partial y \in \mathbb{C}^{MK \times N}$, where

$$\frac{\partial \boldsymbol{a}_{m,k}}{\partial x} = -j\frac{2\pi}{\lambda_k} \boldsymbol{a}_{m,k}(\boldsymbol{p}) \frac{x - x_{\mathrm{Tx},m}}{\|\boldsymbol{p} - \boldsymbol{p}_{\mathrm{Tx},m}\|_2} + \frac{x - x_{\mathrm{Rx},m}}{\|\boldsymbol{p} - \boldsymbol{p}_{\mathrm{Rx},m}\|_2}, \tag{13}$$

$$\frac{\partial \boldsymbol{a}_{m,k}}{\partial y} = -j\frac{2\pi}{\lambda_k} \boldsymbol{a}_{m,k}(\boldsymbol{p}) \frac{y - y_{\mathrm{Tx},m}}{\|\boldsymbol{p} - \boldsymbol{p}_{\mathrm{Tx},m}\|_2} + \frac{y - y_{\mathrm{Rx},m}}{\|\boldsymbol{p} - \boldsymbol{p}_{\mathrm{Rx},m}\|_2}. \tag{14}$$

Therefore, the NLOS part of (10) is approximated as

$$\begin{aligned}\boldsymbol{y}^{\mathrm{NLOS}} &= \boldsymbol{\Phi}\mathbf{A}(\boldsymbol{p} + \Delta\boldsymbol{p})\boldsymbol{x} + \boldsymbol{n} &(15)\\ &\approx \boldsymbol{\Phi}\big(\mathbf{A}(\boldsymbol{p})\boldsymbol{x} + \nabla_{\boldsymbol{p}}\mathbf{A}(\boldsymbol{p})(\Delta\boldsymbol{p} \circ \boldsymbol{x})\big) + \boldsymbol{n} &(16)\\ &= \boldsymbol{\Phi}\big(\mathbf{A}\boldsymbol{x} + \mathbf{A}_x\boldsymbol{s}_x + \mathbf{A}_y\boldsymbol{s}_y\big) + \boldsymbol{n} &(17)\\ &= \tilde{\mathbf{A}}\tilde{\boldsymbol{x}} + \boldsymbol{n}, &(18)\end{aligned}$$

where $\tilde{\mathbf{A}} = \boldsymbol{\Phi}([\mathbf{A}, \mathbf{A}_x, \mathbf{A}_y]) \in \mathbb{C}^{MK \times 3N}$, $\tilde{\boldsymbol{x}}^{\mathsf{T}} = [\boldsymbol{x}^{\mathsf{T}}, \boldsymbol{s}_x^{\mathsf{T}}, \boldsymbol{s}_y^{\mathsf{T}}] \in \mathbb{R}^{3N}$ and $\circ$ represents Hadamard product.[4] Specifically, in (16), the first-order Taylor approximation as in (11) is adopted. In (17), we defined auxiliary variables $\boldsymbol{s}_x = \Delta\boldsymbol{x} \circ \boldsymbol{x}$ and $\boldsymbol{s}_y = \Delta\boldsymbol{y} \circ \boldsymbol{x}$ that incorporate the 2D off-grid offset.

The resulting signal model reveals a strong coupling between the unknown environment parameters and the synchronization errors. Specifically, the measurement matrix depends on the PO matrix $\boldsymbol{\Phi}$, while accurate synchronization in turn relies on the reconstructed environment. This mutual dependency leads to a highly nonconvex and bilinear estimation problem for the scattering vector and the POs, which cannot be efficiently solved by conventional approaches [25]. Therefore, AO remains the most pragmatic framework for such bilinear inverse problems.

To tackle this challenge, as shown in Fig. 3, we adopt a two-stage joint OTA phase synchronization and off-grid imaging method that combines coarse synchronization with iterative refinement. First, an OTA coarse synchronization is performed to provide a stable initialization for subsequent imaging algorithms, as detailed in Section III-A. Based on this initialization, we propose a joint AO framework. Let T denote the iteration index. The algorithm alternates between the following two stages: *(i) Off-Grid Imaging*: given the current PO

[4] The measurements in $\tilde{\mathbf{A}}$ are correlated, but the proposed method does not strictly depend on the irrelevance assumptions of $\tilde{\mathbf{A}}$.

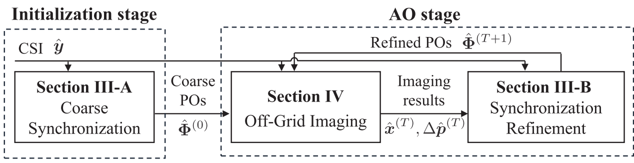

Fig. 3. A sketch of the proposed joint OTA phase synchronization and off-Grid imaging method which iterates between imaging and synchronization during the AO stage.

matrix $\mathbf{\Phi}^{(T)}$, we estimate the environment sparse vector $\hat{\boldsymbol{x}}^{(T)}$ and off-grid offsets $\Delta\hat{\boldsymbol{p}}^{(T)}$ (Section IV); *(ii) Synchronization Refinement*: using the estimated environment parameters from imaging stage as a reference, we update the PO matrix to $\mathbf{\Phi}^{(T+1)}$ (Section III). This process repeats until convergence. In the following sections, we describe the T-th AO iteration in detail.

III. OTA Synchronization Algorithm

In this section, we propose a synchronization procedure consisting of a standard coarse step based on LOS components and an iterative fine synchronization stage, which forms the core contribution. The latter is jointly performed with the OG-AMP imaging algorithm in Section IV under an AO framework to achieve accurate imaging and phase synchronization.

A. Coarse Synchronization

Before AO, to prevent the optimazation result from trapping into a poor local minimum, this stage leverages the LOS path to initialize the synchronization parameters. The received channel frequency response (CFR) $\boldsymbol{y}_m$ for each Tx-Rx link is first transformed into the time domain via an inverse fast Fourier transform (IFFT), yielding a discrete-time channel impulse response. The corresponding power delay profile (PDP) is obtained as the squared magnitude of this time-domain response, i.e., $|\mathrm{IFFT}(\boldsymbol{y}_m)|^2$, which characterizes the signal power distribution over propagation delays. In this section, $\boldsymbol{u}$ is ignored for clarity. For links with a LOS component, we utilize the known node locations to compute the theoretical link delay. The LOS peak search is confined within a local CP window centered at this delay. We further apply a power threshold based on theoretical path loss to filter out the peak. This ensures highly accurate LOS phase extraction. Based on this observation, a time-domain gating operator $\mathcal{T}_m\{\cdot\}$ is applied to isolate the earliest significant delay tap corresponding to the LOS path. The extracted LOS component is then transformed back to the frequency domain as

$$\hat{\boldsymbol{h}}_m^{\mathrm{LOS}} = \mathrm{FFT}\Big(\mathcal{T}_m\Big\{\mathrm{IFFT}(\boldsymbol{y}_m)\Big\}\Big). \tag{19}$$

Using the estimated $\hat{h}_{m,k}^{\mathrm{LOS}}$ and the known ideal $h_{m,k}^{\mathrm{LOS}}$ in (9), the coarse PO is calculated as

$$\hat{\Phi}_{m,k} = \angle\Big(\hat{h}_{m,k}^{\mathrm{LOS}} \cdot (h_{m,k}^{\mathrm{LOS}})^*\Big) \tag{20}$$

$$\approx 2\pi(f_c + k\Delta f)\,\hat{\delta}_{t,m} + \phi_{\mathrm{LO},m}, \tag{21}$$

In (20), since the residual timing offset $\hat{\delta}_{t,m}$ is small, the phase angle $\hat{\Phi}_{m,k}$ can be approximated as a linear superposition of the carrier phase offset $\phi_{\mathrm{LO},m}$ and the frequency-dependent propagation delay. After identifying the dominant peak of the PDP, for example, via cross-correlation with the known pulse-shaping filter, we extract the initial phase $\hat{\Phi}_m$ directly from the corresponding complex observation rather than deriving it from the estimated TOA. The unknown residual phase error $\Delta\Phi_{m,k}$ caused by sampling error after this stage is expressed as the difference between the true and estimated phases,

$$\begin{aligned}\Delta\Phi_{m,k} &= \Phi_{m,k} - \hat{\Phi}_{m,k}\\ &\approx 2\pi(f_c + k\Delta f)(\delta_{t,m} - \hat{\delta}_{t,m}) - 2\pi f_c(\delta_{t,m} - \hat{\delta}_{t,m})\\ &= 2\pi k\Delta f(\delta_{t,m} - \hat{\delta}_{t,m}),\end{aligned} \tag{22}$$

where $\hat{\delta}_{t,m}$ is the time delay corresponding to the estimated LOS path. This approach is inherently robust as it directly captures the large phase rotation $2\pi f_c \delta_{t,m}$ caused by the carrier frequency f_c and the hardware-induced PO $\phi_{\mathrm{LO},m}$. After LOS-based coarse synchronization, residual POs may persist due to limited delay resolution caused by sampling errors and noise in PDP estimation. The accuracy of $\hat{\Phi}_{m,k}$ is mainly constrained by two factors: (i) bandwidth-limited delay resolution, which may cause bias when NLOS paths are not resolvable from the LOS component, and (ii) SNR, which fundamentally limits the accuracy of both the PDP peak location and its complex amplitude. While zero-padding can reduce discretization effects, it cannot overcome these intrinsic limitations. Nevertheless, since the LOS path typically has significantly higher power than NLOS components, the resulting residual phase error is expected to be moderate and provides a sufficiently coherent initialization for subsequent NLOS-aided imaging and fine synchronization. The estimation results in this section provide $\hat{\mathbf{\Phi}}^{(0)} = \mathrm{diag}([e^{-j\hat{\Phi}_{1,1}}, \ldots, e^{-j\hat{\Phi}_{M,K}}]) \in \mathbb{C}^{MK\times MK}$ as a stable initialization for subsequent AO.

For links with a resolvable LOS path, i.e., $u_m = 1$, a coarse estimate of the link-level phase $\Phi_{m,k}$ can be directly obtained from the LOS component. In contrast, for links with $u_m = 0$, no direct phase observation is available at this stage. The available coarse phase observations can be written as

$$\mathrm{diag}(\tilde{\boldsymbol{u}})\boldsymbol{\varphi}_k = \mathrm{diag}(\tilde{\boldsymbol{u}})\mathbf{G}\boldsymbol{\phi}_k. \tag{23}$$

The entries of the link-level phase matrix $\mathbf{G}$ are formed by summing individual Tx and Rx hardware phase offsets, giving $\mathbf{G}$ a rank-one outer-product structure. Importantly, this low-rank structure of $\mathbf{G}$ ensures that all links are constrained through shared Tx/Rx nodes. Consequently, even for links without direct measurements ($u_m = 0$), their phases can still be indirectly and accurately recovered via $\hat{\Phi}_{m,k} = \mathbf{g}_m^{\mathsf{T}}\boldsymbol{\phi}_k$ based on the global structure of $\mathbf{G}$. In cases of severe network occlusion where the geometry matrix becomes heavily incomplete, adopting advanced cooperative synchronization methods [34] or downscaling the network to isolate the disconnected nodes becomes necessary to maintain valid phase initialization.

B. Synchronization Refinement

After the LOS-aided coarse synchronization in Section III-A and the imaging stage in Section IV, a coarse estimate of sparse scattering coefficients $\hat{\boldsymbol{x}}^{(T)}$ and off-grid offsets $\Delta\hat{\boldsymbol{p}}_n^{(T)}$ obtained from estimates of $\boldsymbol{s}_x$ and $\boldsymbol{s}_y$ are available. In this subsection, we exploit the reconstructed environment as a structural reference to refine the residual POs across distributed links. Different from conventional synchronization approaches, the proposed method performs OTA phase synchronization by leveraging the NLOS multipath components to refine the synchronization parameters for the $(T+1)$-th AO iteration. We omit the superscript T for variables within this section unless necessary.

The refined synchronization aims to align the observed CSI with the reconstructed NLOS response by compensating the residual POs. As shown in Fig. 3, refined position $\hat{\boldsymbol{p}} = \boldsymbol{p} + \Delta\hat{\boldsymbol{p}}$ is calculated by adding the estimated off-grid offsets to the grid center. We formulate the refined synchronization problem as maximum likelihood (ML) estimation

$$\hat{\boldsymbol{\Phi}} = \arg\min_{\boldsymbol{\Phi}} \|\boldsymbol{\Phi}^{-1}\hat{\boldsymbol{y}}^{\mathrm{NLOS}} - \tilde{\mathbf{A}}(\hat{\boldsymbol{p}})\hat{\boldsymbol{x}}\|_2^2. \tag{24}$$

Since $\boldsymbol{\Phi}$ is a diagonal matrix, optimization problem (24) can be decomposed into the following ML analytical solution for the m-th link and k-th subcarrier,

$$\hat{\Phi}_{m,k} = \angle\big(\hat{y}_{m,k}^{\mathrm{NLOS}}(h_{m,k}^{\mathrm{NLOS}})^*\big), \tag{25}$$

where $h_{m,k}^{\mathrm{NLOS}} = \sum_{n=1}^{N} a_{m,k}(\hat{\boldsymbol{p}}_n)\hat{x}_n$. According to the node-based phase model in (7), given the ML estimate $\hat{\boldsymbol{\Phi}}_k$ obtained from (24), the node-level phase vector is refined via least squares as

$$\hat{\boldsymbol{\phi}}_k = \big(\mathbf{G}^{\mathsf{T}}\mathbf{G}\big)^{-1}\mathbf{G}^{\mathsf{T}}\hat{\boldsymbol{\varphi}}_k, \tag{26}$$

where $\hat{\boldsymbol{\varphi}}_k = [\hat{\Phi}_{1,k},\ldots,\hat{\Phi}_{M,k}] \in \mathbb{C}^M$. The graph-consistent link phase is then reconstructed as

$$\tilde{\boldsymbol{\varphi}}_k = \mathbf{G}\hat{\boldsymbol{\phi}}_k. \tag{27}$$

Note that since the large-scale synchronization error have already been removed in the first-stage coarse synchronization, the remaining residual phase offsets are tightly bounded within $[-\pi,\pi)$. Physically, (26) and (27) average out random noise by combining multiple link-level observations. Since each node is connected to the network, the matrix $\mathbf{G}$ remains invertible, allowing us to robustly solve for all node-level phases together rather than estimating each link in isolation.

Based on estimated POs, we update the matrix $\boldsymbol{\Phi}^{(T)}$ in (10) for the $(T+1)$-th AO iteration,

$$\boldsymbol{\Phi}^{(T+1)} = \boldsymbol{\Phi}^{(T)} \cdot k_\phi \tilde{\boldsymbol{\Phi}}, \tag{28}$$

where $k_\phi \in (0,1)$ is the damping factor. Matrix $\tilde{\boldsymbol{\Phi}} = \mathrm{diag}([e^{-j\tilde{\varphi}_1},\ldots,e^{-j\tilde{\varphi}_K}]) \in \mathbb{C}^{MK\times MK}$. This updated matrix $\boldsymbol{\Phi}^{(T+1)}$ is then fed back into the OG-AMP algorithm in Section IV to refine the sparse recovery, forming a closed-loop AO.

IV. OG-AMP Algorithm for Imaging

In the T-th AO iteration, the PO matrix $\hat{\boldsymbol{\Phi}}^{(T)}$ is treated as known constant, we omit the superscript T for variables within this section unless necessary. We employ the OG-AMP algorithm to solve for $\boldsymbol{x}$ and off-grid offsets given the observation $\boldsymbol{y}$ and fixed PO $\hat{\boldsymbol{\Phi}}$. After applying the current

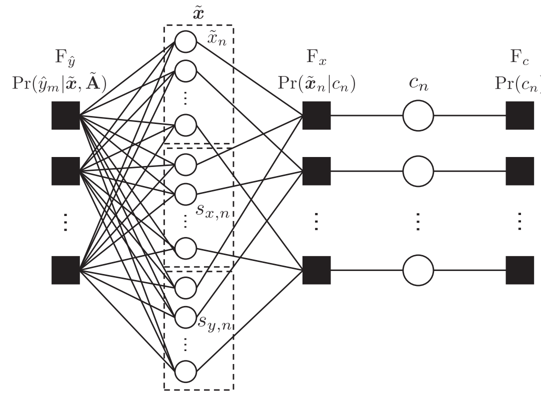

Fig. 4. The factor graph of the OG-AMP algorithm, where squares represent FNs and circles represent VNs.

synchronization, the ideal LOS component is removed from the estimated CSI. Based on (18), the NLOS observation can be written as

$$\begin{aligned}\hat{\boldsymbol{y}}^{\mathrm{NLOS}} &= \hat{\boldsymbol{\Phi}}^{-1}\boldsymbol{y} - \hat{\boldsymbol{h}}^{\mathrm{LOS}} \circ \tilde{\boldsymbol{u}} \\ &= \Delta\boldsymbol{\Phi}\tilde{\mathbf{A}}\tilde{\boldsymbol{x}} + (\Delta\boldsymbol{\Phi} - \mathbf{I})\hat{\boldsymbol{h}}^{\mathrm{LOS}} \circ \tilde{\boldsymbol{u}} + \tilde{\boldsymbol{n}} \\ &\approx \Delta\boldsymbol{\Phi}\tilde{\mathbf{A}}\tilde{\boldsymbol{x}} + \tilde{\boldsymbol{n}},\end{aligned} \tag{29}$$

where $\Delta\boldsymbol{\Phi} = \mathrm{diag}([e^{-j\Delta\Phi_{1,1}},\ldots,e^{-j\Delta\Phi_{M,K}}]) \in \mathbb{C}^{MK\times MK}$ denotes the unknown residual synchronization error matrix defined in (22). Vector $\tilde{\boldsymbol{n}}$ represents Gaussian white noise with variance σ_{n}^2. The second term $(\Delta\boldsymbol{\Phi} - \mathbf{I})\hat{\boldsymbol{h}}^{\mathrm{LOS}}$ represents the residual LOS leakage caused by imperfect synchronization. Since this term enters the model additively and is typically small after coarse synchronization, it can be ignored. In addition, this residual leakage is not fatal to the imaging. Since the LOS path strictly represents the direct propagation between known transceivers, its structural impact during sparse reconstruction is spatially confined, primarily manifesting as a artifact near the antenna positions rather than spreading across the entire ROI [35]. Therefore, the fundamental purpose of performing LOS cancellation here is not to avoid algorithmic divergence, but to remove the excessive LOS energy, so that weak NLOS environmental targets can be revealed.

In this section, we propose an OG-AMP algorithm for the off-grid model in Section II-C, while existing works may alleviate modeling mismatch through pixel modeling, they fundamentally rely on on-grid models and do not explicitly resolve the off-grid nature of physical scatterers [11], [33]. Furthermore, the proposed OG-AMP algorithm improves upon this by absorbing the residual phase synchronization error $\Delta\boldsymbol{\Phi}$ into the estimated complex amplitude and position offset. Even without explicit correction of these residual errors, the sparse structure of the path and the relative positions $\hat{\boldsymbol{s}}_x, \hat{\boldsymbol{s}}_y$ can still be approximately recovered. Therefore, OG-AMP exhibits robustness to PO and can assist in synchronization.

A. Problem Formulation

We consider (29) by ignoring the unknown residual PO estimation error $\Delta\boldsymbol{\Phi}$, the maximum *a posteriori* probability estimate of $\tilde{\boldsymbol{x}}$ is expressed as

$$\hat{\boldsymbol{x}} = \arg\max_{\tilde{\boldsymbol{x}}} \Pr(\tilde{\boldsymbol{x}}|\hat{\boldsymbol{y}}, \tilde{\mathbf{A}}). \tag{30}$$

Note that for clarity, the NLOS superscript of $\hat{\boldsymbol{y}}^{\mathrm{NLOS}}$ in Section IV is omitted. As shown in Fig. 4, we propose a factor graph based on the decomposition result of the joint posterior probability,

$$\Pr(\tilde{\boldsymbol{x}}, \boldsymbol{c}|\hat{\boldsymbol{y}}, \tilde{\mathbf{A}}) \propto \Pr(\hat{\boldsymbol{y}}|\tilde{\boldsymbol{x}}, \tilde{\mathbf{A}}) \Pr(\tilde{\boldsymbol{x}}|\boldsymbol{c}) \Pr(\boldsymbol{c}), \tag{31}$$

where $\boldsymbol{c} \in \mathbb{B}^N$ is an activation index indicating that non-zero elements in $\boldsymbol{x}$, $\boldsymbol{s}_x$, and $\boldsymbol{s}_y$ have the same index. The goal is to compute the posterior probability of c_n and the posterior means of x_n, $s_{x,n}$, and $s_{y,n}$.

We use a factor graph [36] to represent the posterior probability in (31). In Fig. 4, circles represent variable nodes (VNs) $\tilde{\boldsymbol{x}}$ and $\boldsymbol{c}$, and squares represent factor nodes (FNs) $\Pr(\hat{y}_m|\tilde{\boldsymbol{x}}, \tilde{\mathbf{A}})$, $\Pr(\tilde{x}|c_n)$, and $\Pr(c_n)$, whose names are abbreviated as $\mathrm{F}_{\hat{y}}$, F_x, and F_c, respectively. The lines connecting the nodes indicate that these variables are included in the functions of the FNs. The specific functions of FNs are defined as follows:

- FN F_c: Define the sparse prior distribution of scatterers in the environment as $\Pr(c_n) = \eta^{c_n}(1-\eta)^{1-c_n}$, where η is the sparsity, which needs to be roughly set in advance.
- FN F_x: Define the distributions of variables x_n, $s_{x,n}$, and $x_{y,n}$ as

$$\Pr(x_n|c_n) = \begin{cases} \mathcal{CN}(\mu_{x,n}, \sigma^2_{x,n}), & c_n = 1, \\ \delta(x_n), & c_n = 0, \end{cases} \tag{32}$$

$$\Pr(s_{x,n}|c_n) = \begin{cases} \mathcal{CN}(\mu_{s_x,n}, \sigma^2_{s_x,n}), & c_n = 1, \\ \delta(s_x), & c_n = 0, \end{cases} \tag{33}$$

$$\Pr(s_{y,n}|c_n) = \begin{cases} \mathcal{CN}(\mu_{s_y,n}, \sigma^2_{s_y,n}), & c_n = 1, \\ \delta(s_y), & c_n = 0, \end{cases} \tag{34}$$

  where the variable c_n controls whether variables x_n, $s_{x,n}$, and $s_{y,n}$ are activated together, with means $\mu_{x,n}$, $\mu_{s_x,n}$, and $\mu_{s_y,n}$, and variances $\sigma^2_{x,n}$, $\sigma^2_{s_x,n}$, and $\sigma^2_{s_y,n}$, respectively. Note that in the algorithm, we treat x_n as a complex value, which absorbs the common offset caused by synchronization errors, thus enhancing the robustness of the algorithm.
- FN $\mathrm{F}_{\hat{y}}$: $\hat{\boldsymbol{y}}$ can be considered as an observation of $\tilde{\mathbf{A}}\tilde{\boldsymbol{x}}$ under Gaussian noise, $\Pr(\hat{\boldsymbol{y}}|\tilde{\boldsymbol{x}}, \tilde{\mathbf{A}}) = \mathcal{CN}(\tilde{\mathbf{A}}\tilde{\boldsymbol{x}}, \sigma^2_{\mathrm{n}}\mathbf{I})$.

B. Approximate Message Passing

In this section, according to the factor graph, the messages passed iteratively between the VNs and FNs can be derived following the theory of sum-product algorithm [36]. We follows a fundamental assumption of AMP theory [22], we drop some high-order infinitesimal terms. Based on the central limit theorem, when $N \to \infty$, MK/N remains constant, the messages are approximated as Gaussian random variables, thereby calculating the approximate marginal posterior distribution of the unknown variables. Note that all x_n, $s_{x,n}$, and $s_{y,n}$ below are equivalent and their derivations are similar.

1) From FN $\mathrm{F}_{\hat{y}}$ to VN $\tilde{\boldsymbol{x}}$: As derived in Appendix A, the mean and variance of the message $\mu^{(t)}_{\mathrm{F}_{\hat{y},m}\to x_n}(x_n)$ in t-th iteration is updated as

$$\hat{x}^{(t)}_{m\to x_n} = \frac{\hat{y}_m - Z^{(t)}_{m\to x_n}}{a_{m,n}}, \tag{35}$$

$$v^{(t)}_{m\to x_n} = \frac{\sigma^2_{\mathrm{n}} + V^{(t)}_{m\to x_n}}{|a_{m,n}|^2}. \tag{36}$$

The derivations of $s_{x,n}$ and $s_{y,n}$ are similar and will not be repeated here.

2) From VN $\tilde{\boldsymbol{x}}$ to FN F_x: As derived in Appendix B, the mean and variance of the message $\mu^{(t)}_{x_n\to \mathrm{F}_{x,n}}(x_n)$ in t-th iteration is updated as

$$\hat{x}^{(t)}_{n\to \mathrm{F}_x} = v^{(t)}_{n\to \mathrm{F}_x}\left(\sum_{m=1}^{M} \frac{\hat{x}^{(t)}_{m\to x_n}}{v^{(t)}_{m\to x_n}}\right), \tag{37}$$

$$v^{(t)}_{n\to \mathrm{F}_x} = \left(\sum_{m=1}^{M} \frac{1}{v^{(t)}_{m\to x_n}}\right)^{-1}. \tag{38}$$

The derivations of $s_{x,n}$ and $s_{y,n}$ are similar and will not be repeated here.

3) From FN F_x to VN $\boldsymbol{c}$: The message $\mu^{(t)}_{\mathrm{F}_{x,n}\to c_n}(c_n)$ in t-th iteration is expressed as

$$\mu^{(t)}_{\mathrm{F}_{x,n}\to c_n}(c_n) \propto Z^{(t)}_{x,n}(c_n) Z^{(t)}_{s_{x,n}}(c_n) Z^{(t)}_{s_{y,n}}(c_n), \tag{39}$$

where $Z^{(t)}_{x,n}(c_n) = \int \Pr(x_n|c_n)\mu^{(t)}_{x_n\to \mathrm{F}_{x,n}}(x_n)\mathrm{d}x_n$. The definitions of $Z^{(t)}_{s_{x,n}}(c_n)$ and $Z^{(t)}_{s_{y,n}}(c_n)$ are similar and will not be repeated here. As derived in Appendix C, $Z^{(t)}_{x,n}(c_n)$ is calculated as

$$Z^{(t)}_{x,n}(0) = \mathcal{CN}(0; \hat{x}^{(t)}_{n\to \mathrm{F}_x}, v^{(t)}_{n\to \mathrm{F}_x}), \tag{40}$$

$$Z^{(t)}_{x,n}(1) = \mathcal{CN}(\mu_{x,n}; \hat{x}^{(t)}_{n\to \mathrm{F}_x}, \sigma^2_{x,n} + v^{(t)}_{n\to \mathrm{F}_x}). \tag{41}$$

Multiplying the results of $Z^{(t)}_{x,n}(c_n)$, $Z^{(t)}_{s_{x,n}}(c_n)$ and $Z^{(t)}_{s_{y,n}}(c_n)$, we obtain the message passed to c_n.

4) From FN F_c to VN $\boldsymbol{c}$: This message is unrelated to iteration, $\mu_{\mathrm{F}_{c,n}\to c_n}(c_n) = \Pr(c_n)$.

5) From VN $\boldsymbol{c}$ to FN F_x: This message is unrelated to iteration, $\mu_{c_n\to \mathrm{F}_{x,n}}(c_n) \propto \mu_{\mathrm{F}_{c,n}\to c_n}(c_n)$.

6) From FN F_x to VN $\tilde{\boldsymbol{x}}$: As derived in Appendix D, the message $\mu^{(t+1)}_{\mathrm{F}_{x,n}\to x_n}(x_n)$ is approximated to

$$\mu^{(t+1)}_{\mathrm{F}_{x,n}\to x_n}(x_n) \propto k^{(t+1)}_{n,0}\delta(x_n) + k^{(t+1)}_{n,1}\mathcal{CN}(x_n; \mu_{x,n}, \sigma^2_{x,n}), \tag{42}$$

where weights $k^{(t+1)}_{n,0}$ and $k^{(t+1)}_{n,1}$ are defined as

$$k^{(t+1)}_{n,0} \propto (1-\eta)\cdot Z^{(t)}_{s_{x,n}}(0)\cdot Z^{(t)}_{s_{y,n}}(0), \tag{43}$$

$$k^{(t+1)}_{n,1} \propto \eta\cdot Z^{(t)}_{s_{x,n}}(1)\cdot Z^{(t)}_{s_{y,n}}(1). \tag{44}$$

The messages $\mu^{(t+1)}_{\mathrm{F}_{x,n}\to s_{x,n}}$ and $\mu^{(t+1)}_{\mathrm{F}_{x,n}\to s_{y,n}}$ passed to $s_{x,n}$ and $s_{y,n}$ also have the exact same form, only the corresponding weights need to be adjusted accordingly.

7) From VN $\tilde{\boldsymbol{x}}$ to FN $\mathrm{F}_{\hat{y}}$: As derived in Appendix E, the mean and variance in (71) and (72) of the message $\mu^{(t+1)}_{x_n\to \mathrm{F}_{\hat{y},m}}(x_n)$ are approximated to

$$\hat{x}^{(t+1)}_{n\to \mathrm{F}_{\hat{y},m}} = P^{(t+1)}_{n,1\to m}\cdot \hat{x}^{(t+1)}_{\mathrm{prod},m}, \tag{45}$$

$$\begin{aligned} v^{(t+1)}_{n\to \mathrm{F}_{\hat{y},m}} &= P^{(t+1)}_{n,1\to m} v^{(t+1)}_{\mathrm{prod},m} \\ &\quad + \left(P^{(t+1)}_{n,1\to m} - (P^{(t+1)}_{n,1\to m})^2\right)|\hat{x}^{(t+1)}_{\mathrm{prod},m}|^2, \end{aligned} \tag{46}$$

where the normalized weights $P^{(t+1)}_{n,1\to m}$ other intermediate variables are defined in Appendix E. The derivations of $s_{x,n}$ and $s_{y,n}$ are similar and will not be repeated here.

C. Estimation and Iterative Execution

1) Estimation for Active Pixels: In t-th iteration, for each n, calculate the posterior probability of c_n as

$$\Pr(c_n=1|\hat{\boldsymbol{y}},\tilde{\mathbf{A}}) \propto \mu_{\mathrm{F}_{c,n}\to c_n}(1)\cdot \mu^{(t)}_{\mathrm{F}_{x,n}\to c_n}(1) \tag{47}$$

$$\propto \eta\cdot Z^{(t)}_{x,n}(1) Z^{(t)}_{s_{x,n}}(1) Z^{(t)}_{s_{y,n}}(1), \tag{48}$$

$$\Pr(c_n=0|\hat{\boldsymbol{y}},\tilde{\mathbf{A}}) \propto \mu_{\mathrm{F}_{c,n}\to c_n}(0)\cdot \mu^{(t)}_{\mathrm{F}_{x,n}\to c_n}(0) \tag{49}$$

$$\propto (1-\eta)\cdot Z^{(t)}_{x,n}(0) Z^{(t)}_{s_{x,n}}(0) Z^{(t)}_{s_{y,n}}(0). \tag{50}$$

If $\Pr(c_n=1|\hat{\boldsymbol{y}},\tilde{\mathbf{A}})/\big(\Pr(c_n=1|\hat{\boldsymbol{y}},\tilde{\mathbf{A}})+\Pr(c_n=0|\hat{\boldsymbol{y}},\tilde{\mathbf{A}})\big) > \eta_c$, set $\hat{c}^{(t)}_n = 1$. Otherwise, set $\hat{c}^{(t)}_n = 0$. Generally, we set $\eta_c = 0.5$. The set of active pixels in t-th iteration is defined as $\mathcal{A}^{(t)} = \{n|\hat{c}^{(t)}_n = 1\}$.

In this step, a key aspect of the proposed algorithm is that matrices $\mathbf{A}$, $\mathbf{A}_x$ and $\mathbf{A}_y$ are not static during iteration. They are recalculated in each iteration t based on the estimated offset position. At the start of the t-th iteration, we use the offsets $\hat{s}^{(t-1)}_{x,n}$ and $\hat{s}^{(t-1)}_{y,n}$ estimated in the previous $(t-1)$-th iteration to calculate the gradient matrices $\mathbf{A}^{(t)}_x$ and $\mathbf{A}^{(t)}_y$, which effectively reduces the error of the first-order Taylor approximation in (11).

2) Estimation for Scattering Coefficient and Off-Grid Pixel Offsets: For inactive pixels $n \notin \mathcal{A}$: $\hat{x}^{(t)}_n = 0$, $\hat{s}^{(t)}_{x,n} = 0$, $\hat{s}^{(t)}_{y,n} = 0$. For active pixels $n \in \mathcal{A}^{(t)}$, $\Pr(x_n|\hat{\boldsymbol{y}},\tilde{\mathbf{A}}) \propto \mu_{\mathrm{F}_{x,n}\to x_n}(x_n)\cdot\prod_{m=1}^{M}\mu^{(t)}_{\mathrm{F}_{\hat{y},m}\to x_n}(x_n) \propto \mathcal{CN}(x_n;\mu_{x,n},\sigma^2_{x,n})\mathcal{CN}(x_n;\hat{x}^{(t)}_{n\to \mathrm{F}_x}, v^{(t)}_{n\to \mathrm{F}_x})$. The estimated mean $\hat{x}^{(t)}_n$ and variance $v^{(t)}_n$ are

$$\hat{x}^{(t)}_n = v^{(t)}_n\left(\frac{\mu_{x,n}}{\sigma^2_{x,n}} + \frac{\hat{x}^{(t)}_{n\to \mathrm{F}_x}}{v^{(t)}_{n\to \mathrm{F}_x}}\right), \tag{51}$$

$$v^{(t)}_n = \left(\frac{1}{\sigma^2_{x,n}} + \frac{1}{v^{(t)}_{n\to \mathrm{F}_x}}\right)^{-1}. \tag{52}$$

The derivations of $\hat{s}^{(t)}_{x,n}$ and $\hat{s}^{(t)}_{y,n}$ are similar and will not be repeated here.

3) Iterative Execution: The message passing rules derived in Section IV-B define an iterative algorithm. We summarize the proposed OG-AMP algorithm in Algorithm 1. In each iteration of the OG-AMP algorithm, the most computationally intensive operations are matrix-vector multiplications between

Algorithm 1 The proposed OG-AMP Algorithm

Input: The frequency f_k. The positions $\boldsymbol{p}_{\mathrm{Tx}}$, $\boldsymbol{p}_{\mathrm{Rx}}$ and $\boldsymbol{p}$. NLOS channel estimation results $\hat{\boldsymbol{y}}$. Prior probability parameters $\mu_{x,n}$, $\mu_{s_x,n}$, $\mu_{s_y,n}$, $\sigma^2_{x,n}$, $\sigma^2_{s_x,n}$, and $\sigma^2_{s_y,n}$.

1: **Initialization**: Set $\hat{x}^{(0)}_{n\to \mathrm{F}_{\hat{y},m}} = \mu_{x,n}$, $v^{(0)}_{n\to \mathrm{F}_{\hat{y},m}} = \sigma^2_{x,n}$. Set $\hat{s}^{(0)}_{x,n\to \mathrm{F}_{\hat{y},m}}$, $v^{(0)}_{s_x,n\to \mathrm{F}_{\hat{y},m}}$, $\hat{s}^{(0)}_{y,n\to \mathrm{F}_{\hat{y},m}}$, $v^{(0)}_{s_y,n\to \mathrm{F}_{\hat{y},m}}$ similarly. Initialize $\tilde{\mathbf{A}}^{(0)}$ according to (1), (13) and (14).

2: **while** $t < t_{\max}$ and $\|\hat{\boldsymbol{x}}^{(t)} - \hat{\boldsymbol{x}}^{(t-1)}\|/N > \varepsilon$, where ε is a given error tolerance value **do**

3: *Update Messages from FN $\mathrm{F}_{\hat{y}}$ → VN $\tilde{\boldsymbol{x}}$*:
- Calculate $Z^{(t)}_{m\to x_n}$ and $V^{(t)}_{m\to x_n}$ according to (71) and (72). Repeat for $Z^{(t)}_{m\to s_{x,n}}$, $V^{(t)}_{m\to s_{x,n}}$, $Z^{(t)}_{m\to s_{y,n}}$, $V^{(t)}_{m\to s_{y,n}}$.
- Calculate $\hat{x}^{(t)}_{m\to x_n}$ and $v^{(t)}_{m\to x_n}$ according to (35) and (36). Repeat for $\hat{s}^{(t)}_{x,m\to x_n}$, $v^{(t)}_{s_x,m\to x_n}$, $\hat{s}^{(t)}_{y,m\to x_n}$, $v^{(t)}_{s_y,m\to x_n}$.

4: *Update Messages From VN $\tilde{\boldsymbol{x}}$ → FN F_x*:
- Calculate $\hat{x}^{(t)}_{n\to \mathrm{F}_x}$ and $\hat{v}^{(t)}_{n\to \mathrm{F}_x}$ according to (37) and (38).
- Repeat for $\hat{s}^{(t)}_{x,n\to \mathrm{F}_x}$, $v^{(t)}_{s_x,n\to \mathrm{F}_x}$, $\hat{s}^{(t)}_{y,n\to \mathrm{F}_x}$, $v^{(t)}_{s_y,n\to \mathrm{F}_x}$.

5: *Update Messages From FN F_x → VN $\tilde{\boldsymbol{x}}$ → FN $\mathrm{F}_{\hat{y}}$*:
- Calculate terms $Z^{(t)}_{x,n}(0)$ and $Z^{(t)}_{x,n}(1)$ according to (40) and (41). Repeat for $Z^{(t)}_{s_x,n}(0)$, $Z^{(t)}_{s_x,n}(1)$, $Z^{(t)}_{s_y,n}(0)$, $Z^{(t)}_{s_y,n}(1)$.
- Calculate parameters $\hat{x}^{(t)}_{\mathrm{cav},m}$ and $v^{(t)}_{\mathrm{cav},m}$ according to (99) and (100). Repeat for s_x and s_y.
- Calculate parameters $\hat{x}^{(t+1)}_{\mathrm{prod},m}$ and $v^{(t+1)}_{\mathrm{prod},m}$ according to (97) and (98). Repeat for s_x and s_y.
- Calculate weights $k^{(t+1)}_{n,0}$, $k^{(t+1)}_{n,1}$, $W^{(t+1)}_{n,0}$, $W^{(t+1)}_{n,1}$ and $P^{(t+1)}_{n,1\to m}$ according to (43), (44), (95), (96) and (94). Repeat for weights of s_x, s_y.
- Calculate $\hat{x}^{(t+1)}_{n\to \mathrm{F}_{\hat{y},m}}$ and $v^{(t+1)}_{n\to \mathrm{F}_{\hat{y},m}}$ according to (45) and (46). Repeat for $\hat{s}^{(t+1)}_{x,n\to \mathrm{F}_{\hat{y},m}}$, $v^{(t+1)}_{s_x,n\to \mathrm{F}_{\hat{y},m}}$, $\hat{s}^{(t+1)}_{y,n\to \mathrm{F}_{\hat{y},m}}$, $v^{(t+1)}_{s_y,n\to \mathrm{F}_{\hat{y},m}}$.

6: *Estimation and Gradients Update*:
- Estimate $\mathcal{A}^{(t)}$ according to (48) and (50).
- For $n \notin \mathcal{A}^{(t)}$: $\hat{x}^{(t)}_n = 0$, $\hat{s}^{(t)}_{x,n} = 0$, $\hat{s}^{(t)}_{y,n} = 0$. Keep the gradients unchanged: $\mathbf{A}^{(t+1)}(:,n) = \mathbf{A}^{(t)}(:,n)$, $\mathbf{A}^{(t+1)}_x(:,n) = \mathbf{A}^{(t)}_x(:,n)$, $\mathbf{A}^{(t+1)}_y(:,n) = \mathbf{A}^{(t)}_y(:,n)$.
- For $n \in \mathcal{A}(t)$: Estimate $\hat{x}^{\mathrm{final}}_n$ and v^{final}_n according to (51) and (52). Repeat for $\hat{s}^{(t)}_{x,n}$ and $\hat{s}^{(t)}_{y,n}$. Calculate the shift $\Delta\hat{x}^{(t)}_n = \hat{s}^{(t)}_{x,n}/\hat{x}^{(t)}_n$ and repeat for $\Delta\hat{y}^{(t)}_n$. Update $\mathbf{A}^{(t+1)}(:,n)$ and the gradients $\mathbf{A}^{(t+1)}_x(:,n)$ and $\mathbf{A}^{(t+1)}_y(:,n)$ based on the offset position according to (13) and (14).

7: Set $t = t+1$. In each iteration, execute steps 3-5. Every t'-th iteration, also execute step 6.

8: **end while**

Output: Scattering coefficient $\hat{x}^{(t)}_n$ and offsets $\Delta\hat{x}^{(t)}_n$, $\Delta\hat{y}^{(t)}_n$.

the measurement matrix $\tilde{\mathbf{A}}$ and the message vectors. Specifically, the update of messages in step 3 and step 4 requires $\mathcal{O}(MN)$ operations. The calculation of posterior statistics and weights (step 5 and 6) involves element-wise operations with linear complexity $\mathcal{O}(N)$ or $\mathcal{O}(M)$. Consequently, the overall complexity of the imaging stage is $\mathcal{O}(MNK)$. Therefore, the total complexity scales linearly with the number of subcarriers and the pixel number, making the method computationally efficient for large-scale distributed MIMO systems compared to algorithms requiring matrix inversions, such as minimum mean squared error (MMSE) estimation, which scale as $\mathcal{O}((3N)^3)$.

In addition, the synchronization refinement stage requires updating the node-level phase and timing vectors, which involves an matrix inversion scaling as $\mathcal{O}((N_{\mathrm{Tx}}+N_{\mathrm{Rx}})^3)$. Therefore, the total complexity of the complete AO framework is expressed as $\mathcal{O}(MNK+(N_{\mathrm{Tx}}+N_{\mathrm{Rx}})^3)$, which is dominated by the $\mathcal{O}(MNK)$ imaging stage.

V. Theoretical Analysis

In this section, we analyze the system performance under the ideal setting and the practical scenario with synchronization and off-grid errors.

A. Imaging Performance for Perfect Synchronization

Consider the ideal scenario with perfect synchronization ($\mathbf{\Phi}=\mathbf{I}$) and no off-grid offsets $\Delta\boldsymbol{p}=\mathbf{0}$, we will demonstrate the impact of basic parameter settings on system performance. The imaging model reduces to $\boldsymbol{y}=\mathbf{A}\boldsymbol{x}+\boldsymbol{n}$, where $\mathbf{A}\in\mathbb{C}^{MK\times N}$ is the measurement matrix and $\boldsymbol{x}$ is an s-sparse vector. Although the measurement matrix $\mathbf{A}$ is structured and not i.i.d. Gaussian, it has been widely observed in ISAC, radar imaging, and compressed sensing literature that the columns of $\mathbf{A}$ behave approximately uncorrelated when the number of measurements MK is large. Stable sparse recovery is guaranteed when the number of measurements satisfies the classical compressed sensing scaling $MK\geq Cs\log(N/s)$ where C is a constant which depends on the RIP level of $\mathbf{A}$, as derived in [20], [25], and [37]. Under this condition, the reconstruction error is expressed as

$$\mathrm{E}\left[\|\hat{\boldsymbol{x}}-\boldsymbol{x}\|_2^2\right]\propto\sigma_{\mathrm{n}}^2\,\frac{\eta\log N}{MK}. \tag{53}$$

Eq. (53) serves as an ideal benchmark for the subsequent analysis. It indicates that increasing the number of links M or subcarriers K improves reconstruction accuracy, while higher sparsity level and noise variance σ_{n}^2 lead to increased estimation error.

B. Synchronization Performance Bound for Perfect Imaging

In the proposed method, residual POs are modeled through a node-based phase estimation. After LOS-aided coarse synchronization and imaging, the refined synchronization stage estimates the link-level phases and then projects them onto the node-consistent subspace. In this subsection, we analyze the performance bound of estimating the node-level phase parameters $\boldsymbol{\phi}_k$ and discuss their impact on imaging performance.

1) CRB for PO Estimation: Assuming perfect imaging, the received CSI for link m and subcarrier k is $y_{m,k}=e^{-j\phi_{m,k}}h_{m,k}+n_{m,k}$, where $h_{m,k}$ is the ideal channel coefficient and $n_{m,k}\sim\mathcal{CN}(0,\sigma_{\mathrm{n}}^2)$. Using the sufficient statistic $z_{m,k}=\angle\big(y_{m,k}(h_{m,k})^*\big)=\phi_{m,k}+w_{m,k}$, the effective phase noise $w_{m,k}$ can be approximated at high SNR as

$$\mathrm{Var}(w_{m,k})\approx\frac{\sigma_{\mathrm{n}}^2}{2|h_{m,k}|^2}. \tag{54}$$

Stacking all M links at subcarrier k, we obtain the linear Gaussian model $\boldsymbol{z}_k=\mathbf{G}\boldsymbol{\phi}_k+\boldsymbol{\eta}_k$, where $\boldsymbol{\eta}_k$ has diagonal covariance matrix $\mathbf{\Sigma}_k=\mathrm{diag}(\sigma_{m,k}^2)$ with $\sigma_{m,k}^2=\mathrm{Var}(w_{m,k})$. The Fisher information matrix for $\boldsymbol{\phi}_k$ is therefore given by $\mathbf{J}_k=\mathbf{G}^\mathsf{T}\mathbf{\Sigma}_k^{-1}\mathbf{G}$, and the corresponding CRB is $\mathbf{J}_k^{-1}$. To reveal the impact of NLOS propagation, note that

$$|h_{m,k}|^2=\Big|\sum_{n\in\mathcal{A}}a_{m,k}(\boldsymbol{p}_n+\Delta\boldsymbol{p}_n)x_n\Big|^2. \tag{55}$$

Therefore, the CRB is approximated as

$$\mathrm{CRB}(\boldsymbol{\phi}_k)\propto\frac{\sigma_{\mathrm{n}}^2}{|\mathcal{A}|}\left(\mathbf{G}^\mathsf{T}\mathbf{G}\right)^{-1}. \tag{56}$$

It can be concluded that the estimation accuracy of node-level phase parameters is jointly determined by the network topology encoded in $\mathbf{G}$, the effective signal strength of reconstructed NLOS components $|\mathcal{A}|$, and the presence of residual phase errors. A well-connected network topology improves the conditioning of $\mathbf{G}^\mathsf{T}\mathbf{G}$, thereby significantly reducing the CRB. Moreover, spatially diverse NLOS multipath components enhance the effective SNR of phase observations, which further improves synchronization accuracy. This analysis explains why exploiting NLOS multipath as a structural reference is essential for achieving reliable OTA synchronization in distributed MIMO ISAC systems.

2) Impact on Imaging Performance: After node-level phase refinement, the residual estimation error $\Delta\boldsymbol{\phi}_k=\boldsymbol{\phi}_k-\hat{\boldsymbol{\phi}}_k$ induces a structured residual phase error on each link, $\Delta\boldsymbol{\varphi}_k=\mathbf{G}\Delta\boldsymbol{\phi}_k$. For small residual errors, the resulting multiplicative distortion can be linearized as $e^{-j\Delta\varphi_{m,k}}\approx1-j\Delta\varphi_{m,k}$, which converts the phase error into an additive perturbation on the measurement matrix. The equivalent noise variance induced by node-level synchronization errors is expressed as

$$\begin{aligned}\sigma_{\mathrm{syn}}^2&\approx\mathrm{E}\left[(\Delta\varphi_{m,k})^2\right]|h_{m,k}|^2 &(57)\\&=|h_{m,k}|^2\left[\mathbf{G}\mathbf{J}_k^{-1}\mathbf{G}^\mathsf{T}\right]_{m,m} &(58)\\&\propto\frac{\sigma_{\mathrm{n}}^2}{|\mathcal{A}|}|h_{m,k}|^2\left[\mathbf{G}(\mathbf{G}^\mathsf{T}\mathbf{G})^{-1}\mathbf{G}^\mathsf{T}\right]_{m,m}. &(59)\end{aligned}$$

This expression reveals how node-level phase uncertainty propagates to link-level distortions and degrades the measurement SNR. As a result, synchronization accuracy, network topology, and the number of available subcarriers jointly determine the imaging performance.

C. Off-Grid Approximation Error

In this subsection, we will analyze the impact of residuals on performance caused by the linear approximation of the off-grid offset. The second-order remainder in the first-order Taylor expansion (11) is given by

$$\varepsilon_{m,k}^{\text{off}} = \frac{1}{2}\Delta \boldsymbol{p}_n^{\mathsf{T}}\, \nabla_{\boldsymbol{p}}^2 a_{m,k}(\boldsymbol{p}_n)\, \Delta \boldsymbol{p}_n, \tag{60}$$

For propagation over frequency f_k, we obtain $\nabla_{\boldsymbol{p}}^2 a_{m,k} \sim \left(\frac{2\pi}{\lambda_k}\right)^2 a_{m,k}$. Substituting into the remainder, we give the off-grid error as

$$\mathrm{E}\left[|\varepsilon_{m,k}^{\text{off}}|^2\right] \propto \left(\frac{2\pi}{\lambda_k}\right)^4 \mathrm{E}\left[\|\Delta \boldsymbol{p}_n\|_2^4\right]. \tag{61}$$

With total subcarriers K, the total off-grid distortion is expressed as

$$\sigma_{\text{off}}^2 \propto \frac{1}{K}\sum_{k=1}^{K}\left(\frac{2\pi}{\lambda_k}\right)^4 \mathrm{E}[\|\Delta \boldsymbol{p}_n\|_2^4]. \tag{62}$$

After polynomial expansion, the dominant term is governed by the carrier wavelength λ_c, and we approximate $\lambda_k^4 \approx \lambda_c^4$. Assuming that the off-grid displacement $\Delta \boldsymbol{p}_n$ is uniformly distributed within a square pixel of side length d_{pixel}, the resulting variance of the off-grid approximation error can be expressed as

$$\sigma_{\text{off}}^2 \propto \frac{1}{K}\left(\frac{1}{\lambda_c}\right)^4 d_{\text{pixel}}^4. \tag{63}$$

We conclude that the off-grid error increases with λ_c^{-4} and the fourth power of the pixel size, while decreasing with the number of subcarriers. While extending this framework to mmWave or THz bands would require finer grid resolutions to compensate for smaller wavelengths λ_c, the relative computational efficiency of the proposed OG-AMP algorithm over baseline methods [24], [25] remains valid.

VI. Numerical Results

In this section, we evaluate the performance of the proposed NLOS-aided joint OTA synchronization and off-grid imaging framework through numerical simulations. The effectiveness of the proposed method is demonstrated in terms of synchronization accuracy and imaging performance. We also provide a comparison with the benchmark scheme OMP [21] and GAMP [22]. Compared to OMP, GAMP demonstrates stronger robustness and performance in the compressed sensing reconstruction problem with non-strict Gaussian measurement matrices and it is therefore used as a representative baseline method for our evaluation [33].

A. Simulation Setting and Metrics

Unless otherwise specified, all simulation parameters are fixed as follows, except for the variable under study in each performance curve. We consider a distributed MIMO ISAC system with $N_{\text{Tx}} = 30$ Txs and $N_{\text{Rx}} = 30$ Rxs randomly deployed around the 2D ROI. All nodes are fully connected and have LOS paths. In imaging stage, the ROI is discretized into $N = 25 \times 25$ pixels, with a grid spacing of 0.2 m in both dimensions. The carrier frequency is set to $f_c = 1$ GHz and the subcarrier spacing is $\Delta f = 120$ kHz. During the coarse synchronization stage, a full OFDM bandwidth consisting of multiple contiguous subcarriers can be used to enable reliable LOS delay estimation. In our simulation, the LOS signal components are assumed to be estimated and subtracted from the received signals during the coarse synchronization stage. After coarse synchronization is completed, two representative subcarriers are selected for the subsequent AO-based imaging and fine synchronization process. This is motivated by the fact that imaging resolution in the considered distributed MIMO setup is mainly determined by the effective spatial aperture rather than the bandwidth, so a small number of subcarriers is sufficient while reducing computational complexity.

Each Tx–Rx pair suffers from unknown residual POs after coarse synchronization as described in Section III-A. Based on (22), the residual POs of the first subcarrier are generated according to a zero-mean Gaussian distribution with standard deviation $\sigma_\phi = 0.2\pi$. The noise is modeled as complex Gaussian with variance σ_{n}^2 corresponding to an SNR of 25 dB unless otherwise specified. The proposed AO framework iteratively performs off-grid imaging and OTA synchronization. The maximum number of AO iterations is set to 10, and the error tolerance in the OG-AMP algorithm is set to $\varepsilon = 10^{-4}$. Damping factor $k_\phi \in (0,1)$ is set to 0.3. The prior probability settings for OG-AMP are as follows: $\mu_{x,n} = 1$, $\mu_{s_x,n} = 0$, $\mu_{s_y,n} = 0$, $\sigma_{x,n} = 0.1$. The standard deviations $\sigma_{s_x,n}$, $\sigma_{s_y,n}$ are set to half the pixel size.

Since both the ground truth and the imaging results are off-grid, chamfer distance (CD) is used to measure the spatial accuracy of the imaging results,

$$\begin{aligned} d_{\text{CD}}(\mathcal{X}, \hat{\mathcal{X}}) = &\frac{1}{|\mathcal{X}|}\sum_{\mathbf{p}(x)\in\mathcal{X}} \min_{\mathbf{p}(\hat{x})\in\hat{\mathcal{X}}} \|\mathbf{p}(x) - \mathbf{p}(\hat{x})\|_2^2 \\ &+ \frac{1}{|\hat{\mathcal{X}}|}\sum_{\mathbf{p}(\hat{x})\in\hat{\mathcal{X}}} \min_{\mathbf{p}(x)\in\mathcal{X}} \|\mathbf{p}(\hat{x}) - \mathbf{p}(x)\|_2^2, \end{aligned} \tag{64}$$

where $\mathcal{X}$ and $\hat{\mathcal{X}}$ are pixel sets of the ground truth and imaging results and $\mathbf{p}(\cdot)$ denotes the spatial coordinate of the pixel. A smaller d_{CD} indicates a closer match between the two pixel sets. Root mean squared error (RMSE) is used to measure the synchronization accuracy, $\text{RMSE} = \frac{1}{MK}\left\|\ln \boldsymbol{\Phi} - \ln \hat{\boldsymbol{\Phi}}\right\|_{\text{F}}$, where $\boldsymbol{\Phi}$ and $\hat{\boldsymbol{\Phi}}$ denote the true and estimated POs and $\|\cdot\|_{\text{F}}$ represent the Frobenius norm. Considering the periodicity of the phase, unwrapping is required.

B. Performance Evaluation

Fig. 5 shows the intuitive results of both the baseline and the proposed methods. To clearly illustrate the details, we have set up a toy example with $N_{\text{Tx}} = 10$ Txs and $N_{\text{Rx}} = 10$ Rxs deployed in a $2\text{m} \times 2\text{m}$ ROI. The red crosses in the figure represent the location of the ground truth, and the heatmap represents the imaging results. Fig. 5(a) through (d) illustrates that even under ideal conditions, OMP struggles to achieve a complete and accurate reconstruction. Off-grid errors and POs completely degrade the reconstruction results. Fig. 5(e) through (h) illustrate that while standard GAMP algorithms can achieve good on-grid imaging performance when the target is perfectly centered in the grid, the off-grid effect and the presence of PO greatly degrade the performance. Fig. 5(i)

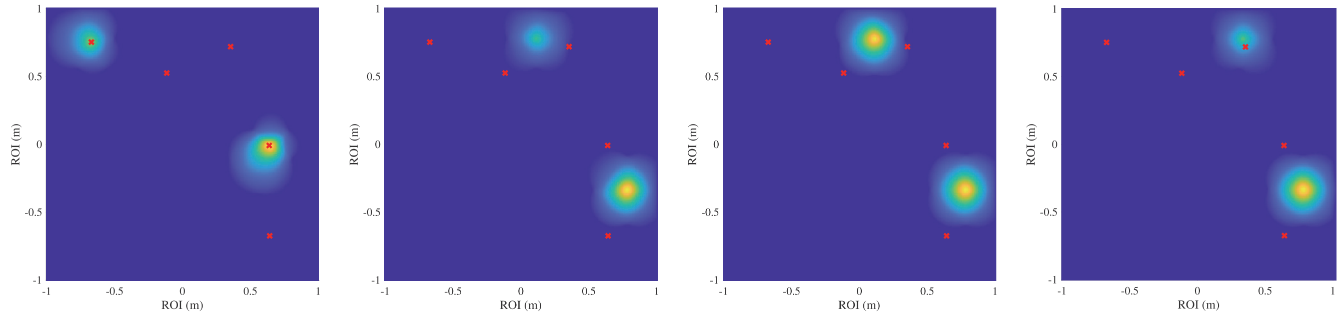

(a) On-grid imaging with OMP, no PO. (CD = 0.1843 m) (b) On-grid imaging with OMP, PO presented. (CD = 0.3241 m) (c) Off-grid imaging with OMP, no PO. (CD = 0.3241 m) (d) Off-grid imaging with OMP, PO presented. (CD = 0.3009 m)

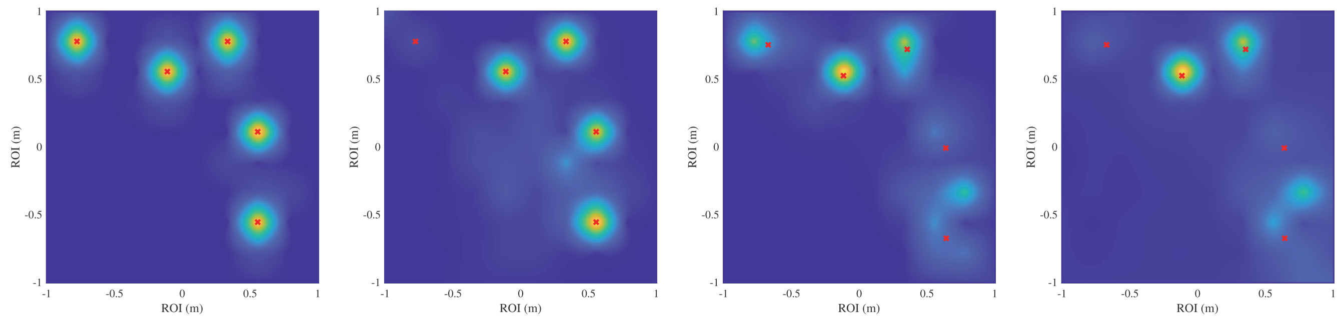

(e) On-grid imaging with GAMP, no PO. (CD = 0.0375 m) (f) On-grid imaging with GAMP, PO presented. (CD = 0.1120 m) (g) Off-grid imaging with GAMP, no PO. (CD = 0.1612 m) (h) Off-grid imaging with GAMP, PO presented. (CD = 0.1854 m)

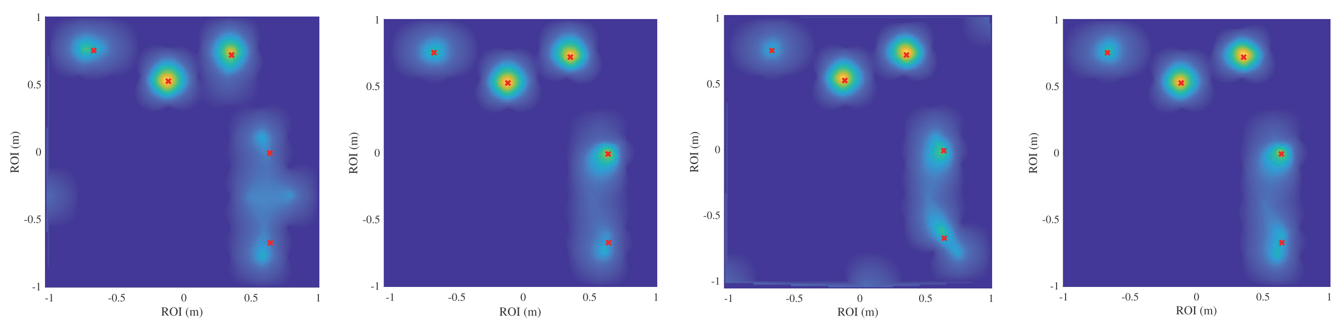

(i) Off-grid imaging with OG-AMP, no PO, without gradient update. (CD = 0.1144 m) (j) Off-grid imaging with OG-AMP, no PO, with gradient update. (CD = 0.0413 m) (k) Off-grid imaging with OG-AMP, PO presented, without AO. (CD = 0.1395 m) (l) Off-grid imaging with OG-AMP, PO presented, with AO. (CD = 0.0453 m)

Fig. 5. The imaging results of OMP, GAMP and the proposed OG-AMP method. (a)-(d): The performance degradation of OMP by POs and off-grid offsets. (e)-(h): The performance degradation of GAMP by POs and off-grid offsets. (i)-(j): Effectiveness of OG-AMP iteration and gradient update. (k)-(l): Effectiveness of AO iteration.

and (j) illustrate the OG-AMP algorithm effectively solves the off-grid imaging problem, based on the gradient update in step 6. Fig. 5(k) and (l) illustrate that the proposed AO algorithm effectively eliminates the influence of PO, making the imaging performance close to the ideal case. Since OMP methods are sensitive to matrix structures and struggle with non-strict Gaussian measurement matrices induced by physical channels and off-grid offsets, it failed to yield valid reconstruction results in this high-resolution imaging setup. Therefore, performance curves are omitted.

Fig. 6 illustrates the system performance of the baseline and the proposed algorithms under different SNRs. The baseline GAMP algorithm is implemented with the off-grid model proposed in Section II-C; otherwise, it would fail to operate in the presence of off-grid errors. As analyzed in Section V-B, the overall system performance improves with increasing SNR. In Fig. 6(a), the proposed AO algorithm effectively eliminates the influence of PO, making the imaging performance close to the ideal case. In Fig. 6(b), the CRBs are obtained through simulations assuming perfect imaging results. It can be observed that the imaging performance of the baseline GAMP algorithm is insufficient to support NLOS-aided synchronization. In contrast, when PO are present, the proposed AO-based methods consistently outperform the conventional approaches.

C. Robustness and Convergence Evaluation

Fig. 7 illustrates the system performance under varying pixel sizes, which validates the spatial discretization analysis in Section V-B. Since the total number of grid points is fixed, increasing the pixel size expands the ROI but simultaneously scales up the maximum potential off-grid displacement. As

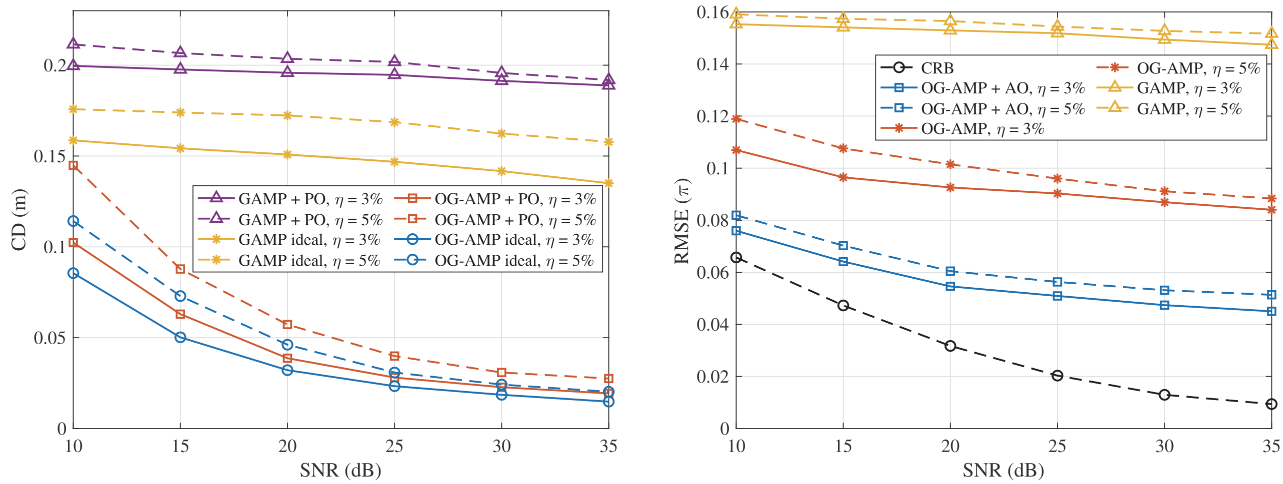

(a) CD of imaging results: After AO, the imaging performance of the PO (red) is close to the perfect calibrated imaging performance (blue).

(b) Estimated RMSE of PO: Comparing the red and blue curves, AO effectively improves synchronization performance.

Fig. 6. The relationship between the SNR and system performance: Overall system performance improves with increasing SNR. CRB curve: Estimating PO based on perfect imaging.

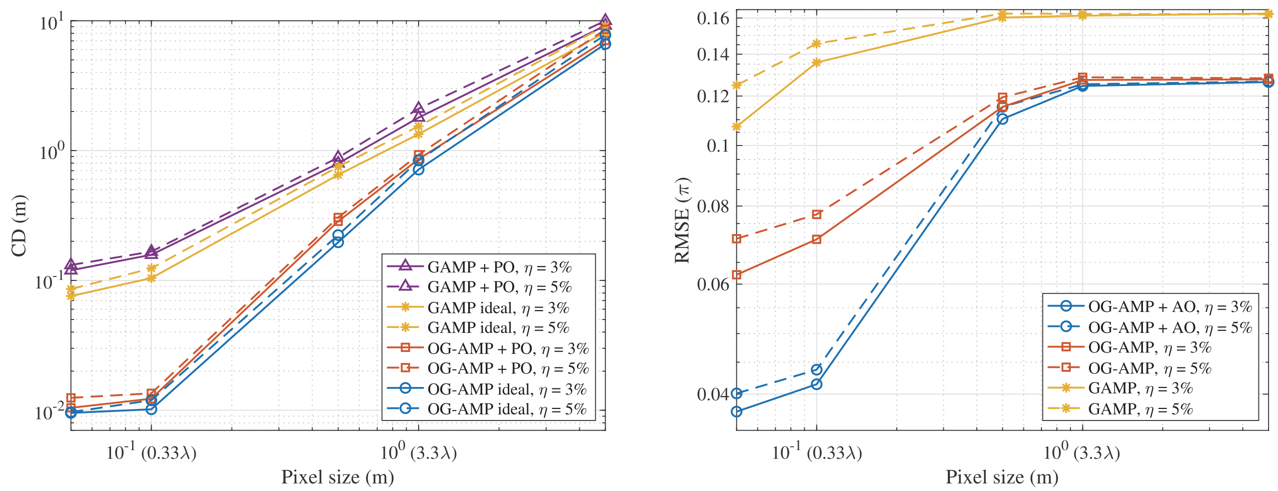

(a) CD of imaging results: The proposed algorithm has better imaging performance.

(b) Estimated RMSE of PO: The proposed AO algorithm supports larger pixel sizes.

Fig. 7. The relationship between the pixel size and system performance.

theoretically derived in Section V-B, larger off-grid errors severe the mismatch in the sensing dictionary, degrading the imaging accuracy and propagating errors into the synchronization loop. Despite this inherent physical performance loss, the proposed algorithm consistently outperforms the baseline methods, proving its superior capability in solving larger grid mismatches.

Fig. 8 illustrates the impact of POs to verify the synchronization error analysis in Section V-B. It can be observed that larger initial POs distort the phase coherence of the received signals, degrading the imaging accuracy, which in turn leads to performance loss in synchronization. In addition, Fig. 8 compares the imaging performance at carrier frequencies of 1 GHz and 5 GHz. For a fair comparison, at 5 GHz, the pixel size for the 5 GHz carrier is set to 4 cm. It can be seen that increasing the carrier frequency improves system performance. However, as analyzed in Section V-C, the pixel size must be reduced to mitigate the off-grid offset. While conventional computational imaging methods fail under severe POs, our approach exhibits robustness, maintaining a stable performance even with significant residual POs.

Fig. 9 illustrates the convergence of the proposed AO algorithm, where the number of iterations is slightly increased for clearer illustration. Fig. 9(a) illustrates that the OG-AMP imaging algorithm also shows fast convergence. However, due to the iteratively gradient updates in step 6, the residual in step 2 continues to decrease slowly. Because phase offsets and off-grid offsets are non-linearly coupled, this phenomenon represents a localized joint refinement where both variables cooperatively adjust within tiny residual phase bounds. Nevertheless, this refinement does not lead to further improvement in the overall system performance. Therefore, an appropriate stopping threshold ε should be selected to avoid unnecessary iterations. As shown in Figs. 9(b) and 9(c), the system performance converges rapidly within a few AO iterations.

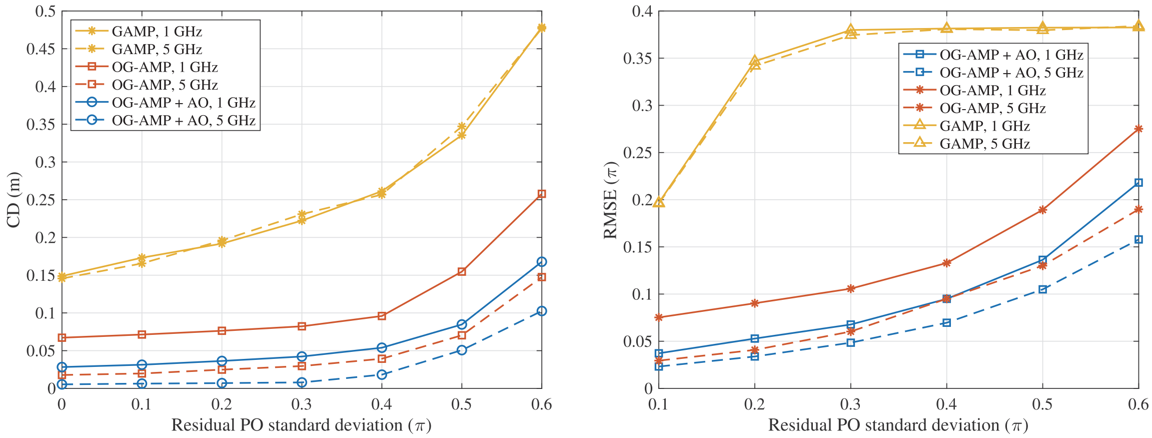

(a) CD of imaging results: The proposed algorithm exhibits better robustness against PO.

(b) Estimated RMSE of PO: The conventional algorithm fail quickly, but the proposed algorithm remains robust.

Fig. 8. The relationship between the residual PO and system performance. x-axis: Standard deviation σ_ϕ of residual PO estimation error after coarse synchronization. y-axis: Imaging and refinement synchronization performance in AO.

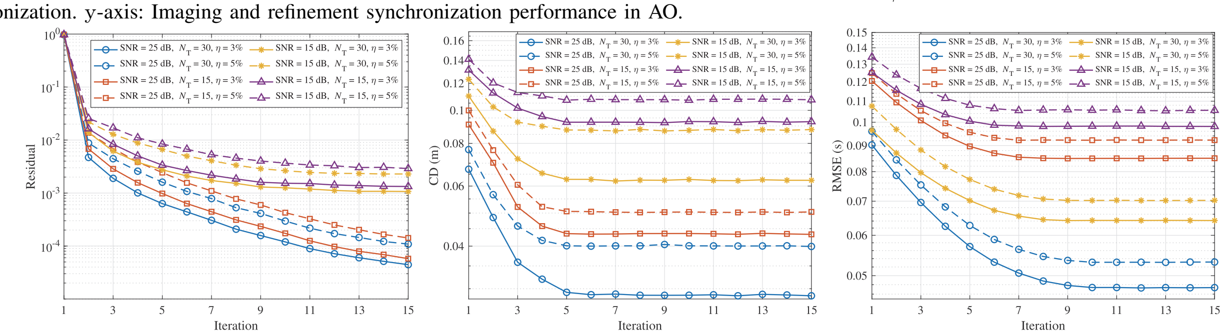

(a) The convergence performance of OG-AMP.

(b) The convergence performance in CD.

(c) The convergence performance in PO.

Fig. 9. The convergence performance of joint synchronization and imaging. (a): The gradient update in the OG-AMP algorithm with t iterations. (b)-(c): Imaging and synchronization in AO with T iterations.

VII. Conclusion

This paper proposed an NLOS-aided joint framework for OTA phase synchronization and off-grid imaging in distributed MIMO ISAC systems. Based on LOS-assisted coarse synchronization, a unified ISAC framework is proposed by combining off-grid computational imaging with NLOS-assisted refined synchronization within a closed-loop AO framework. Analytical results provided insights into the impact of carrier frequency, bandwidth, and grid resolution on off-grid modeling errors. Numerical simulations demonstrated that the proposed approach achieves accurate synchronization and imaging under POs. These results highlight the robustness and practical applicability of the proposed method for large-scale distributed ISAC systems. Future work will extend this framework to handle extended targets and partial LOS blockages. Adapting the algorithm to continuous shapes rather than point targets is also a viable and important next step to improve robustness in complex environments.

Appendix A
Approximation of Message $\mu^{(t)}_{\mathrm{F}_{\hat{y},m}\to x_n}(x_n)$

According to Fig. 4, the message $\mu^{(t)}_{\mathrm{F}_{\hat{y},m}\to x_n}(x_n)$ can be expressed as

$$\mu^{(t)}_{\mathrm{F}_{\hat{y},m}\to x_n}(x_n) \propto \int \Pr(\hat{y}_m|\tilde{\boldsymbol{x}},\tilde{\mathbf{A}}) \prod_{i\neq n} \mu^{(t)}_{x_i\to\mathrm{F}_{\hat{y},m}}(x_i)\mathrm{d}x_i \prod_{l=1}^{N} \mu^{(t)}_{s_{x,l}\to\mathrm{F}_{\hat{y},m}}(s_{x,l})\mathrm{d}s_{x,l} \prod_{l=1}^{N} \mu^{(t)}_{s_{y,l}\to\mathrm{F}_{\hat{y},m}}(s_{y,l})\mathrm{d}s_{y,l}. \quad (65)$$

We isolate the x_n term,

$$\hat{y}_m = a_{m,n}x_n + \Big(\sum_{j\neq n} a_{m,j}x_j + \sum_{l=1}^{N} a^{(t)}_{x,m,l}s_{x,l} + \sum_{l=1}^{N} a^{(t)}_{y,m,l}s_{y,l} + n_m\Big) \quad (66)$$

$$= a_{m,n}x_n + S^{(t)}_{m\to x_n}, \quad (67)$$

where $S^{(t)}_{m\to x_n}$ is a sum of many random variables, the distribution of each variable j is given by its incoming message $\mu^{(t)}_{j\to\mathrm{F}_{\hat{y},m}}$. Following the standard assumption ($M, N \to \infty, M/N = \mathrm{const}$) in belief propagation for such models, we apply the central limit theorem. We approximate this entire sum as a complex Gaussian random variable. The message is simplified to

$$\mu^{(t)}_{\mathrm{F}_{\hat{y},m}\to x_n}(x_n) \propto \int \mathcal{CN}(\hat{y}_m; a_{m,n}x_n + S^{(t)}_{m\to x_n}, \sigma_{\mathrm{n}}^2) \Pr(S^{(t)}_{m\to x_n})\mathrm{d}S^{(t)}_{m\to x_n} \quad (68)$$

$$\approx \int \mathcal{CN}(\hat{y}_m; a_{m,n}x_n + S^{(t)}_{m\to x_n}, \sigma_{\mathrm{n}}^2)$$

$$\mathcal{CN}(S^{(t)}_{m\to x_n}; Z^{(t)}_{m\to x_n}, V^{(t)}_{m\to x_n})\mathrm{d}S^{(t)}_{m\to x_n} \quad (69)$$

$$\propto \mathcal{CN}(x_n; \hat{x}^{(t)}_{m\to x_n}, v^{(t)}_{m\to x_n}), \quad (70)$$

where $\hat{x}^{(t)}_{m\to x_n}$ and $v^{(t)}_{m\to x_n}$ are the mean and variance of $\mu^{(t)}_{\mathrm{F}_{\hat{y},m}\to x_n}(x_n)$ as calculated in (35) and (36). The mean $Z^{(t)}_{m\to x_n}$ and variance $V^{(t)}_{m\to x_n}$ of $S^{(t)}_{m\to x_n}$ are calculated as

$$Z^{(t)}_{m\to x_n} = \sum_{j\neq n} a_{m,j}\hat{x}^{(t)}_{j\to \mathrm{F}_{\hat{y},m}} + \sum_{l=1}^{N} a^{(t)}_{x,m,l}\hat{s}^{(t)}_{x,l\to \mathrm{F}_{\hat{y},m}} + \sum_{l=1}^{N} a^{(t)}_{y,m,l}\hat{s}^{(t)}_{y,l\to \mathrm{F}_{\hat{y},m}}, \quad (71)$$

$$V^{(t)}_{m\to x_n} = \sum_{j\neq n} |a_{m,j}|^2 v^{(t)}_{j\to \mathrm{F}_{\hat{y},m}} + \sum_{l=1}^{N} |a^{(t)}_{x,m,l}|^2 v^{(t)}_{x,l\to \mathrm{F}_{\hat{y},m}} + \sum_{l=1}^{N} |a^{(t)}_{y,m,l}|^2 v^{(t)}_{y,l\to \mathrm{F}_{\hat{y},m}}, \quad (72)$$

where $\hat{x}^{(t)}_{j\to \mathrm{F}_{\hat{y},m}}$ and $v^{(t)}_{j\to \mathrm{F}_{\hat{y},m}}$ are the mean and variance of the message $\mu^{(t)}_{x_j\to \mathrm{F}_{\hat{y},m}}(x_j)$, which will be derived later.

Appendix B
Approximation of Message $\mu^{(t+1)}_{\mathrm{F}_{x,n}\to x_n}(x_n)$

The message $\mu^{(t)}_{x_n\to \mathrm{F}_{x,n}}(x_n)$ in t-th iteration is approximated as

$$\mu^{(t)}_{x_n\to \mathrm{F}_{x,n}}(x_n) \propto \prod_{m=1}^{M} \mu^{(t)}_{\mathrm{F}_{\hat{y},m}\to x_n}(x_n) \quad (73)$$

$$= \prod_{m=1}^{M} \mathcal{CN}(x_n; \hat{x}^{(t)}_{m\to x_n}, v^{(t)}_{m\to x_n}) \quad (74)$$

$$\propto \mathcal{CN}(x_n; \hat{x}^{(t)}_{n\to \mathrm{F}_x}, v^{(t)}_{n\to \mathrm{F}_x}), \quad (75)$$

where $\hat{x}^{(t)}_{n\to \mathrm{F}_x}$ and $v^{(t)}_{n\to \mathrm{F}_x}$ are the mean and variance of $\mu^{(t)}_{x_n\to \mathrm{F}_{x,n}}(x_n)$, then we obtain (37) and (38).

Appendix C
Derivation of $Z^{(t)}_{x,n}(c_n)$

When $c_n = 1$: $\Pr(x_n|c_n = 1) = \mathcal{CN}(x_n; \mu_{x,n}, \sigma^2_{x,n})$ and $\mu^{(t)}_{x_n\to \mathrm{F}_{x,n}}(x_n) \propto \mathcal{CN}(x_n; \hat{x}^{(t)}_{n\to \mathrm{F}_x}, v^{(t)}_{n\to \mathrm{F}_x})$, we obtain

$$Z^{(t)}_{x,n}(1) = \int \mathcal{CN}(x_n; \mu_{x,n}, \sigma^2_{x,n}) \mathcal{CN}(x_n; \hat{x}^{(t)}_{n\to \mathrm{F}_x}, v^{(t)}_{n\to \mathrm{F}_x})\mathrm{d}x_n \quad (76)$$

$$= \mathcal{CN}(\mu_{x,n}; \hat{x}^{(t)}_{n\to \mathrm{F}_x}, \sigma^2_{x,n} + v^{(t)}_{n\to \mathrm{F}_x}). \quad (77)$$

When $c_n = 0$: $\Pr(x_n|c_n = 0) = \delta(x_n)$, we obtain

$$Z^{(t)}_{x,n}(0) = \int \delta(x_n)\mathcal{CN}(x_n; \hat{x}^{(t)}_{n\to \mathrm{F}_x}, v^{(t)}_{n\to \mathrm{F}_x})\mathrm{d}x_n \quad (78)$$

$$= \mathcal{CN}(0; \hat{x}^{(t)}_{n\to \mathrm{F}_x}, v^{(t)}_{n\to \mathrm{F}_x}). \quad (79)$$

Appendix D
Approximation of Message $\mu^{(t+1)}_{\mathrm{F}_{x,n}\to x_n}(x_n)$

The message $\mu^{(t+1)}_{\mathrm{F}_{x,n}\to x_n}(x_n)$ in $(t+1)$-th iteration is expressed as

$$\mu^{(t+1)}_{F_{x,n}\to x_n}(x_n) = \sum_{c_n\in\{0,1\}} \Pr(x_n|c_n)\mu_{c_n\to \mathrm{F}_{x,n}}(c_n) Z^{(t)}_{s_{x,n}}(c_n) Z^{(t)}_{s_{y,n}}(c_n), \quad (80)$$

where $Z^{(t)}_{s_{x,n}}(c_n)$ and $Z^{(t)}_{s_{y,n}}(c_n)$ are defined in (39). The derivations of $s_{x,n}$ and $s_{y,n}$ are similar.

When $c_n = 1$: $\Pr(x_n|c_n = 1) = \mathcal{CN}(x_n; \mu_{x,n}, \sigma^2_{x,n})$ and $\mu_{c_n\to \mathrm{F}_{x,n}}(1) \propto \eta$, we obtain the term in (80),

$$\mathrm{Term}_1 = \mathcal{CN}(x_n; \mu_{x,n}, \sigma^2_{x,n}) \cdot \eta \cdot Z^{(t)}_{s_{x,n}}(1) \cdot Z^{(t)}_{s_{y,n}}(1). \quad (81)$$

When $c_n = 0$: $\Pr(x_n|c_n = 0) = \delta(x_n)$ and $\mu_{c_n\to \mathrm{F}_{x,n}}(0) \propto (1-\eta)$, we obtain the term in (80),

$$\mathrm{Term}_0 = \delta(x_n) \cdot (1-\eta) \cdot Z^{(t)}_{s_{x,n}}(0) \cdot Z^{(t)}_{s_{y,n}}(0). \quad (82)$$

Define weights as (43) and (44), the passed message from FN F_x to VN $\tilde{\boldsymbol{x}}$ is calculated as the sum of above terms, then we obtain (42).

Appendix E
Approximation of Message $\mu^{(t+1)}_{x_n\to \mathrm{F}_{\hat{y},m}}(x_n)$

The message $\mu^{(t+1)}_{x_n\to \mathrm{F}_{\hat{y},m}}(x_n)$ in $(t+1)$-th iteration is approximated as

$$\mu^{(t+1)}_{x_n\to \mathrm{F}_{\hat{y},m}}(x_n) \propto \mu^{(t+1)}_{\mathrm{F}_{x,n}\to x_n}(x_n) \cdot \prod_{k\neq m} \mu^{(t)}_{\mathrm{F}_{\hat{y},k}\to x_n}(x_n), \quad (83)$$

where

$$\prod_{k\neq m} \mu^{(t)}_{\mathrm{F}_{\hat{y},k}\to x_n}(x_n) \propto \frac{\mu^{(t)}_{x_n\to \mathrm{F}_{x,n}}(x_n)}{\mu^{(t)}_{\mathrm{F}_{\hat{y},m}\to x_n}(x_n)} \quad (84)$$

$$\propto \frac{\mathcal{CN}(x_n; \hat{x}^{(t)}_{n\to \mathrm{F}_x}, v^{(t)}_{n\to \mathrm{F}_x})}{\mathcal{CN}(x_n; \hat{x}^{(t)}_{m\to x_n}, v^{(t)}_{m\to x_n})} \quad (85)$$

$$\propto \mathcal{CN}(x_n; \hat{x}^{(t)}_{\mathrm{cav},m}, v^{(t)}_{\mathrm{cav},m}). \quad (86)$$

The mean $\hat{x}^{(t)}_{\mathrm{cav},m}$ and $v^{(t)}_{\mathrm{cav},m}$ variance are calculated in (99) and (100). Plug (42) and (86) into (83), we obtain

$$\mu^{(t+1)}_{x_n\to \mathrm{F}_{\hat{y},m}}(x_n) \propto \left[k^{(t+1)}_{n,0}\delta(x_n) + k^{(t+1)}_{n,1}\mathcal{CN}(x_n; \mu_{x,n}, \sigma^2_{x,n})\right] \mathcal{CN}(x_n; \hat{x}^{(t)}_{\mathrm{cav},m}, v^{(t)}_{\mathrm{cav},m}) \quad (87)$$

$$\propto W^{(t+1)}_{n,0} \cdot \delta(x_n) + W^{(t+1)}_{n,1} \cdot \mathcal{CN}(x_n; \hat{x}^{(t+1)}_{\mathrm{prod},m}, v^{(t+1)}_{\mathrm{prod},m}), \quad (88)$$

where weights $W^{(t+1)}_{n,0}$ and $W^{(t+1)}_{n,1}$ are calculated in (95) and (96). The mean $\hat{x}^{(t+1)}_{\mathrm{prod},m}$ and variance $v^{(t+1)}_{\mathrm{prod},m}$ are calculated in (97) and (98). Based on the normalized weights $P^{(t+1)}_{n,1\to m}$ defined in (94), the mean and variance of message $\mu^{(t+1)}_{x_n\to \mathrm{F}_{\hat{y},m}}(x_n)$ are derived as

$$\hat{x}^{(t+1)}_{n\to \mathrm{F}_{\hat{y},m}} = P^{(t+1)}_{n,0\to m} \cdot \mathrm{E}[\delta(x_n)] + P^{(t+1)}_{n,1\to m}$$

$$\begin{aligned}
&\mathrm{E}[\mathcal{CN}(x_n;\hat{x}^{(t+1)}_{\mathrm{prod},m},v^{(t+1)}_{\mathrm{prod},m})] && (89)\\
&= P^{(t+1)}_{n,1\to m}\cdot\hat{x}^{(t+1)}_{\mathrm{prod},m}, && (90)\\
v^{(t+1)}_{n\to \mathrm{F}_{\hat{y},m}} &= \mathrm{E}[|x_n|^2]-|\mathrm{E}[x_n]|^2 && (91)\\
&= \left[P^{(t+1)}_{n,1\to m}(v^{(t+1)}_{\mathrm{prod},m}+|\hat{x}^{(t+1)}_{\mathrm{prod},m}|^2)\right]\\
&\quad -\left[(P^{(t+1)}_{n,1\to m})^2|\hat{x}^{(t+1)}_{\mathrm{prod},m}|^2\right] && (92)\\
&= P^{(t+1)}_{n,1\to m}v^{(t+1)}_{\mathrm{prod},m}\\
&\quad +\left(P^{(t+1)}_{n,1\to m}-(P^{(t+1)}_{n,1\to m})^2\right)|\hat{x}^{(t+1)}_{\mathrm{prod},m}|^2. && (93)
\end{aligned}$$

where the normalized weights $P^{(t+1)}_{n,1\to m}$ is calculated as

$$P^{(t+1)}_{n,1\to m}=\frac{W^{(t+1)}_{n,1}}{W^{(t+1)}_{n,0}+W^{(t+1)}_{n,1}}. \tag{94}$$

Weights $W^{(t+1)}_{n,0}$ and $W^{(t+1)}_{n,1}$ are defined as

$$W^{(t+1)}_{n,0}\propto k^{(t+1)}_{n,0}\cdot\mathcal{CN}(0;\hat{x}^{(t)}_{\mathrm{cav},m},v^{(t)}_{\mathrm{cav},m}), \tag{95}$$

$$W^{(t+1)}_{n,1}\propto k^{(t+1)}_{n,1}\cdot\mathcal{CN}(\mu_{x,n};\hat{x}^{(t)}_{\mathrm{cav},m},\sigma^2_{x,n}+v^{(t)}_{\mathrm{cav},m}). \tag{96}$$

Means $\hat{x}^{(t+1)}_{\mathrm{prod},m}$, $\hat{x}^{(t)}_{\mathrm{cav},m}$, and variances $v^{(t+1)}_{\mathrm{prod},m}$, $v^{(t)}_{\mathrm{cav},m}$ are defined as

$$\hat{x}^{(t+1)}_{\mathrm{prod},m}=v^{(t+1)}_{\mathrm{prod},m}\left(\frac{\mu_{x,n}}{\sigma^2_{x,n}}+\frac{\hat{x}^{(t)}_{\mathrm{cav},m}}{v^{(t)}_{\mathrm{cav},m}}\right), \tag{97}$$

$$v^{(t+1)}_{\mathrm{prod},m}=\left(\frac{1}{\sigma^2_{x,n}}+\frac{1}{v^{(t)}_{\mathrm{cav},m}}\right)^{-1}, \tag{98}$$

$$\hat{x}^{(t)}_{\mathrm{cav},m}=v^{(t)}_{\mathrm{cav},m}\left(\frac{\hat{x}^{(t)}_{n\to \mathrm{F}_x}}{v^{(t)}_{n\to \mathrm{F}_x}}-\frac{\hat{x}^{(t)}_{m\to x_n}}{v^{(t)}_{m\to x_n}}\right), \tag{99}$$

$$v^{(t)}_{\mathrm{cav},m}=\left(\frac{1}{v^{(t)}_{n\to F_x}}-\frac{1}{v^{(t)}_{m\to x_n}}\right)^{-1}. \tag{100}$$

REFERENCES

[1] F. Liu et al., "Integrated sensing and communications: Toward dual-functional wireless networks for 6G and beyond," *IEEE J. Sel. Areas Commun.*, vol. 40, no. 6, pp. 1728–1767, Jun. 2022.

[2] Z. Behdad, Ö. T. Demir, K. W. Sung, E. Björnson, and C. Cavdar, "Multi-static target detection and power allocation for integrated sensing and communication in cell-free massive MIMO," *IEEE Trans. Wireless Commun.*, vol. 23, no. 9, pp. 11580–11596, Sep. 2024.

[3] K. Han, K. Meng, and C. Masouros, "Over-the-air time-frequency synchronization in distributed ISAC systems," 2025, *arXiv:2503.08920*.

[4] Y. Wu, M. F. Keskin, U. Gustavsson, G. Seco-Granados, E. G. Larsson, and H. Wymeersch, "Location and map-assisted wideband phase and time calibration between distributed antennas," in *Proc. IEEE Globecom Workshops (GC Wkshps)*, Dec. 2024, pp. 1–6.

[5] E. Björnson and L. Sanguinetti, "Scalable cell-free massive MIMO systems," *IEEE Trans. Commun.*, vol. 68, no. 7, pp. 4247–4261, Jul. 2020.

[6] J. Aguilar, D. Werbunat, V. Janoudi, C. Bonfert, and C. Waldschmidt, "Uncoupled digital radars creating a coherent sensor network," *IEEE J. Microw.*, vol. 4, no. 3, pp. 459–472, Jul. 2024.

[7] U. K. Ganesan, R. Sarvendranath, and E. G. Larsson, "BeamSync: Over-the-air synchronization for distributed massive MIMO systems," *IEEE Trans. Wireless Commun.*, vol. 23, no. 7, pp. 6824–6837, Jul. 2024.

[8] M. Koivisto et al., "Joint device positioning and clock synchronization in 5G ultra-dense networks," *IEEE Trans. Wireless Commun.*, vol. 16, no. 5, pp. 2866–2881, May 2017.

[9] E. G. Larsson, "Massive synchrony in distributed antenna systems," *IEEE Trans. Signal Process.*, vol. 72, pp. 855–866, 2024.

[10] J. Pegoraro et al., "JUMP: Joint communication and sensing with unsynchronized transceivers made practical," *IEEE Trans. Wireless Commun.*, vol. 23, no. 8, pp. 9759–9775, Aug. 2024.

[11] X. Tong, Z. Zhang, Z. Yang, Y. Ge, and H. Wymeersch, "Computational imaging-based ISAC method with large pixel division," in *Proc. IEEE Int. Conf. Commun.*, Jun. 2025, pp. 4511–4516.

[12] F. Dai, H. Fu, L. Hong, L. Li, and H. Liu, "Off-grid error and amplitude–phase drift calibration for computational microwave imaging with metasurface aperture based on sparse Bayesian learning," *IEEE Trans. Geosci. Remote Sens.*, vol. 60, 2022, Art. no. 5115514.

[13] F. Liu, C. Masouros, A. P. Petropulu, H. Griffiths, and L. Hanzo, "Joint radar and communication design: Applications, state-of-the-art, and the road ahead," *IEEE Trans. Commun.*, vol. 68, no. 6, pp. 3834–3862, Jun. 2020.

[14] H. Bi, D. Zhu, G. Bi, B. Zhang, W. Hong, and Y. Wu, "FMCW SAR sparse imaging based on approximated observation: An overview on current technologies," *IEEE J. Sel. Topics Appl. Earth Observ. Remote Sens.*, vol. 13, pp. 4825–4835, 2020.

[15] J. Che, Z. Zhang, H. Zhang, Z. Yang, L. Liu, and C. Huang, "A novel framework for user positioning and environment sensing during initial random access," *IEEE Trans. Wireless Commun.*, vol. 24, no. 2, pp. 1193–1206, Feb. 2025.

[16] M. Manzoni et al., "Wavefield networked sensing: Principles, algorithms, and applications," *IEEE Open J. Commun. Soc.*, vol. 6, pp. 181–197, 2025.

[17] D. Tagliaferri et al., "Cooperative coherent multistatic imaging and phase synchronization in networked sensing," *IEEE J. Sel. Areas Commun.*, vol. 42, no. 10, pp. 2905–2921, Oct. 2024.

[18] A. Liu et al., "A survey on fundamental limits of integrated sensing and communication," *IEEE Commun. Surveys Tuts.*, vol. 24, no. 2, pp. 994–1034, 2nd Quart., 2022.

[19] B. Sun et al., "3D computational imaging with single-pixel detectors," *Science*, vol. 340, no. 6134, pp. 844–847, May 2013.

[20] E. J. Candes et al., "Decoding by linear programming," *IEEE Trans. Inf. Theory*, vol. 51, no. 12, pp. 4203–4215, Dec. 2005.

[21] J. A. Tropp and A. C. Gilbert, "Signal recovery from random measurements via orthogonal matching pursuit," *IEEE Trans. Inf. Theory*, vol. 53, no. 12, pp. 4655–4666, Dec. 2007.

[22] S. Rangan, "Generalized approximate message passing for estimation with random linear mixing," in *Proc. IEEE ISIT*, Jul. 2011, pp. 2168–2172.

[23] Z. Lin et al., "A compressive sensing approach for MIMO-OFDM-based integrated sensing and communication," in *Proc. IEEE GLOBECOM*, Dec. 2023, pp. 522–527.

[24] X. Tong, Z. Zhang, J. Wang, C. Huang, and M. Debbah, "Joint multi-user communication and sensing exploiting both signal and environment sparsity," *IEEE J. Sel. Topics Signal Process.*, vol. 15, no. 6, pp. 1409–1422, Nov. 2021.

[25] X. Tong et al., "Environment sensing considering the occlusion effect: A multi-view approach," *IEEE Trans. Signal Process.*, vol. 70, pp. 3598–3615, 2022.

[26] C. Bryant, L. Patton, B. Rigling, and B. Himed, "Calibration of distributed MIMO radar systems," *IEEE Trans. Radar Syst.*, vol. 3, pp. 124–134, 2025.

[27] O. Kanhere and T. S. Rappaport, "Map-assisted millimeter wave and terahertz position location and sensing," *IEEE Trans. Wireless Commun.*, vol. 24, no. 6, pp. 5323–5336, Jun. 2025.

[28] Y. Li, S. Chen, and W. Meng, "Bilinear approximate message passing based off-grid channel estimation for multi-user millimeter-wave MIMO system," in *Proc. IEEE 96th Veh. Technol. Conf. (VTC-Fall)*, Sep. 2022, pp. 1–6.

[29] L. Zhang, X. Lei, Y. Xiao, W. Zhao, and M. Liu, "A novel message passing detector for block-wise index modulation aided OTFS communications," in *Proc. IEEE Global Commun. Conf. (GLOBECOM)*, Dec. 2024, pp. 4768–4773.

[30] J.-J. van de Beek et al., "On channel estimation in OFDM systems," in *Proc. IEEE 45th VTC*, vol. 2, Jul. 1995, pp. 815–819.

[31] A. Goldsmith, *Wireless Communications*. Cambridge, U.K.: Cambridge Univ. Press, 2005.

[32] Z. Xing, Z. Zhang, X. Tong, Z. Yang, and C. Huang, "Physics-inspired target shape detection and reconstruction in mmWave communication systems," in *Proc. IEEE Global Commun. Conf.*, Dec. 2023, pp. 3910–3915.

[33] X. Tong, Z. Zhang, Z. Yang, Y. Ge, and H. Wymeersch, "Distributed multi-view environment sensing in wireless communication networks," *IEEE Trans. Wireless Commun.*, vol. 25, pp. 12016–12033, 2026.
[34] M. Rashid and J. A. Nanzer, "Frequency and phase synchronization in distributed antenna arrays based on consensus averaging and Kalman filtering," *IEEE Trans. Wireless Commun.*, vol. 22, no. 4, pp. 2789–2803, Apr. 2023.
[35] X. Tong et al., "Integrated sensing, communication, and positioning in cellular vehicular networks," *IEEE Trans. Veh. Technol.*, vol. 75, no. 3, pp. 5274–5279, Mar. 2026.
[36] F. R. Kschischang, B. J. Frey, and H.-A. Loeliger, "Factor graphs and the sum-product algorithm," *IEEE Trans. Inf. Theory*, vol. 47, no. 2, pp. 498–519, Feb. 2001.
[37] R. Baraniuk, M. Davenport, R. DeVore, and M. Wakin, "A simple proof of the restricted isometry property for random matrices," *Constructive Approximation*, vol. 28, no. 3, pp. 253–263, Dec. 2008.

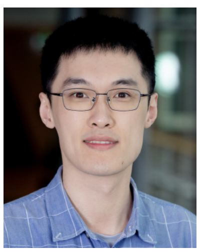

Xin Tong (Member, IEEE) received the B.S. degree from Ningbo University, Ningbo, China, in 2020, and the Ph.D. degree from Zhejiang University, Hangzhou, China, in 2025, under the supervision of Prof. Zhaoyang Zhang. He is currently a Post-Doctoral Researcher with the Department of Electrical Engineering, Chalmers University of Technology, Gothenburg, Sweden. His research interests include integrated sensing and communication, signal processing, and distributed MIMO.

Lechen Zhang (Graduate Student Member, IEEE) received the B.E. degree in communication engineering and the Ph.D. degree in information and communication engineering from the University of Electronic Science and Technology of China, Chengdu, China, in 2020 and 2026, respectively. His current research interests include wireless communications, compressed sensing, and integrated sensing and communication.

Yu Ge (Member, IEEE) received the B.E. degree from Zhejiang University, Hangzhou, China, in 2017, the M.Sc. degree from the KTH Royal Institute of Technology, Stockholm, Sweden, in 2019, and the Ph.D. degree from Chalmers University of Technology, Sweden, in 2024. He was a Post-Doctoral Researcher with the Department of Electrical Engineering, Chalmers University of Technology. His research interests include integrated communication and sensing, wireless positioning systems, simultaneous localization and mapping, and multi-object tracking, particularly in 5G and beyond 5G scenarios.

Dario Tagliaferri (Member, IEEE) received the M.Sc. degree (Hons.) in telecommunication engineering and the Ph.D. degree in information technology from Politecnico di Milano, Italy, in 2015 and 2019, respectively. He is currently a tenure-track Assistant Professor with the Dipartimento di Elettronica, Informazione e Bioingegneria (DEIB). His research interests comprise signal processing techniques for wireless communication and sensing systems, specifically integrated sensing and communication systems, networked sensing, and radio imaging and related synchronization aspects. He holds four patents in the field of signal processing for communication and sensing and three best paper awards. He serves as an Associate Editor for IEEE TRANSACTIONS ON WIRELESS COMMUNICATIONS.

Henk Wymeersch (Fellow, IEEE) received the Ph.D. degree in electrical engineering/applied sciences from Ghent University, Belgium, in 2005. He is currently a Professor of communication systems with the Department of Electrical Engineering, Chalmers University of Technology, Sweden, and a Distinguished Visiting Professor with Tsinghua University. Prior to joining Chalmers, he was a Post-Doctoral Researcher with the Laboratory for Information and Decision Systems, Massachusetts Institute of Technology, from 2005 to 2009. His research interests include the convergence of communication and sensing, in a 5G and beyond 5G context. He is a Senior Member of *IEEE Signal Processing Magazine* Editorial Board. He served as an Associate Editor for IEEE COMMUNICATIONS LETTERS, IEEE TRANSACTIONS ON WIRELESS COMMUNICATIONS, and IEEE TRANSACTIONS ON COMMUNICATIONS. From 2019 to 2021, he was an IEEE Distinguished Lecturer with the Vehicular Technology Society.